

Self-consistent theory of 2×2 pair density waves in kagome superconductors

Meng Yao,¹ Yan Wang,¹ Da Wang,^{1,2,*} Jia-Xin Yin,^{3,†} and Qiang-Hua Wang^{1,2,‡}

¹National Laboratory of Solid State Microstructures & School of Physics, Nanjing University, Nanjing 210093, China

²Collaborative Innovation Center of Advanced Microstructures, Nanjing University, Nanjing 210093, China

³Department of Physics, Southern University of Science and Technology, Shenzhen, Guangdong 518005, China

Pair density wave (PDW) is an intriguing quantum matter proposed in the frontier of condensed matter physics. However, the existence of PDW in microscopic models has been rare. In this work, we obtain, by Ginzburg-Landau arguments and self-consistent mean field theory, novel $2a_0 \times 2a_0$ PDW on the kagome lattice arising from attractive on-bond pairing interactions and the distinct Bloch wave functions near the p-type van Hove singularity. The PDW state carrying three independent wave-vectors, the so-called 3Q PDW, is nodeless and falls into two topological classes characterized by the Chern number $C = 0$ or $C = \pm 2$. The chiral ($C = \pm 2$) PDW state presents a rare case of interaction driven topological quantum state without the requirement of spin-orbit coupling. Finally, we analyze the stabilities and properties of these PDWs intertwining with charge orders, and discuss the relevance of our minimal model to recent experimental observations in kagome superconductors. Our theory not only elucidates the driving force of the chiral PDW, but also predicts strongly anisotropic superconducting gap structure in the momentum space and quantized transverse thermal conductivity that can be tested in future experiments.

Introduction. Pair density wave (PDW) is an exotic superconducting (SC) order with spatially nonuniform order parameters caused by condensing the Cooper pairs with nonzero center of mass momenta. It was first conceived to exist in superconductors with a strong spin-exchange field such that two paired equal-energy electrons do not have opposite momenta anymore [1, 2]. Such a SC state is called FFLO state and has possibly been realized in cold atom systems [3–5]. On the other hand, in cuprates without time-reversal symmetry breaking, the PDW with nonzero pairing momentum has also been proposed phenomenologically to serve as a mother state to generate various daughter states, dubbed as intertwined orders, in the pseudogap phase [6–8]. Such a proposal subsequently triggered extensive studies of PDW in recent years [7, 8], and some signatures of the PDW states have been reported in a series of materials such as cuprate and iron-based superconductors [9–22], heavy fermion material UTe₂ [23, 24], kagome compound AV₃Sb₅ [25], and other materials [26, 27]. Although many theoretical successes have been achieved at the phenomenological level [28–35], the existence of spontaneous PDW is rare in microscopic models, since the usual Cooper pairing with zero momentum always enjoys perfect Fermi surface (FS) nesting in the particle-particle channel and thus leaves no room for PDW, unless the interactions are strong enough to break this weak-coupling picture of Cooper instability. Extensive efforts have been made [36–68], but the existence of long-range PDW order has not been conclusively demonstrated in realistic models.

In this work, we show that the PDW is favored by on-bond pairing interactions on the kagome lattice near the upper p-type van Hove (vH) filling. The resulting

$2a_0 \times 2a_0$ PDW ground states and Bogoliubov-de Gennes (BdG) quasiparticles are analyzed within the Ginzburg-Landau (GL) and self-consistent mean field calculations. Interestingly, such PDW states are found to intertwine with the charge density wave (CDW) orders and are likely to exist in the kagome superconductors AV₃Sb₅, which are intensively studied in the past few years [69–76].

PDW instability near upper vH filling. We study the kagome lattice as shown in Fig. 1(a), with the three sublattices labeled by A, B, and C, respectively. From the tight-binding Hamiltonian

$$H_0 = -t \sum_{\langle ij \rangle \sigma} (c_{i\sigma}^\dagger c_{j\sigma} + \text{H.c.}), \quad (1)$$

with only the nearest neighbor hopping t (taken as energy unit), the band structure is shown in Fig. 1(b). There are two vH fillings $(4 \pm 1)/12$, as indicated by the two dashed lines corresponding to chemical potential $\mu = 0$ and -2 , respectively. For these fillings, their FSs are exactly the same but their Bloch wave functions are quite different. For the upper vH filling as shown in Fig. 1(c), the wave function at each M -point is contributed by purely one sublattice, hence, called p-type. Instead, for the lower vH filling as shown in Fig. 1(d), the wave function at each M is contributed by mixing two sublattices, hence called m-type. The difference between these two vH fillings leads to distinct properties as discussed in previous studies [61, 77–83]. Here, we show that the particular p-type vH singularity can lead to PDW instability instead of the usual SC. If the onsite pairing interaction is suppressed by *e.g.* Hubbard repulsion, the leading pairing interaction is expected to be on the nearest neighbor bond. For this reason, by choosing the basis of on-bond fermion pairs $b_{iI} = c_{i+\delta, \sigma} c_{i+\delta', \sigma'}$ (indices other than unitcell position i are grouped into I), we calculate the zero-frequency bare pairing susceptibility $\hat{\chi}(\mathbf{q})$ with the matrix element $\chi_{IJ}(\mathbf{q}) = \frac{1}{L^d} \sum_{ij} \int_0^\beta d\tau \langle b_{iI}(\tau) b_{jJ}^\dagger(0) \rangle e^{i\mathbf{q} \cdot (\mathbf{r}_j - \mathbf{r}_i)}$. For each \mathbf{q} , we diagonalize $\hat{\chi}(\mathbf{q})$ to obtain its eigenvalues and

* dawang@nju.edu.cn

† yinjax@sustech.edu.cn

‡ qhwang@nju.edu.cn

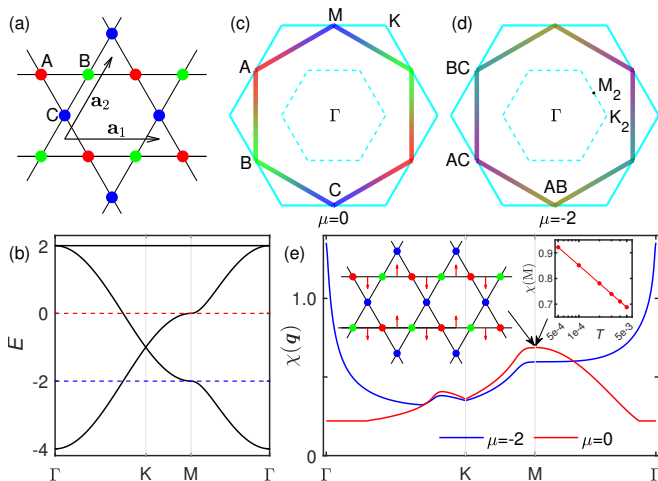


FIG. 1. (a) Kagome lattice structure with the three sublattices labeled by A (red), B (green) and C (blue), respectively. \mathbf{a}_1 and \mathbf{a}_2 denote two primitive translation vectors with length a_0 . (b) Band dispersion along Γ -K-M- Γ , with the red and blue dashed lines indicating two vH fillings. The FS at the upper vH filling is plotted in (c) in the first Brillouin zone (BZ) with color-scaled sublattice weight. The folded BZ for the $2a_0 \times 2a_0$ unitcell is given by dashed lines. (d) is similar to (c) but for the lower vH filling. (e) The largest spin-singlet pairing susceptibility $\chi(\mathbf{q})$ for upper (red) and lower (blue) vH fillings at temperature $T = 0.005$. For one M -point at the upper vH filling, the left inset illustrates the eigen mode with arrow directions (lengths) representing the pairing phases (amplitudes) for relevant bonds (up to a global phase), and the right inset shows the logarithmic temperature dependence of $\chi(M)$.

eigenvectors. The leading eigenvalue $\chi(\mathbf{q})$ in spin-singlet channel at the upper vH filling is plotted in Fig. 1(e). One can see that the highest peak occurs at M , which diverges logarithmically with decreasing temperature (see right inset), indicating the PDW instability with $2a_0 \times 2a_0$ period. This instability is caused by the divergence of the dressed susceptibility $\chi/(1-g\chi)$ at finite temperature for any nonzero attraction g in this pairing channel, as a direct generalization of the Cooper mechanism. Note that for the p-type vH filling, the on-bond pairings only combine different sublattices corresponding to different M -points, and thus carry a finite momentum $\mathbf{M}_3 = \mathbf{M}_1 + \mathbf{M}_2$ (mod reciprocal vectors). This is a new feature in the kagome lattice, which is different from previous studies of PDW with on-bond pairings [43, 48]. The eigenvector at one M is illustrated in the left inset of Fig. 1(e). The arrows indicate the pairing phases (up to a global one) on the relevant bonds. The eigen modes at the other two M -points can be obtained by C_3 rotations. As a comparison, we also plot the susceptibility at the lower vH filling in Fig. 1(e), where the divergence occurs at Γ , indicating the usual SC ground state with zero momentum.

PDW ground states and BdG quasiparticles. The above analysis indicates three degenerate PDW modes at different M -points, which can be associated with three

order parameters $\psi_{1,2,3}$, respectively. Their interplay will lead to different PDW ground states. In terms of $\psi_{1,2,3}$, we construct a three-component GL free energy up to the fourth order by requiring the following symmetries: C_3 -rotation, momentum conservation, time reversal (TR) and U(1) gauge symmetries. Under these constraints, the second order term can only be $|\psi_i|^2$, and the fourth order terms can be $|\psi_i|^4$, $|\psi_i|^2|\psi_j|^2$ and $(\psi_i^{*2}\psi_j^2 + \text{c.c.})$. Note that there is no third order term, as such a term would violate the U(1) gauge symmetry. (See Sec. IV in Supplementary Material [84] for microscopic derivation of the GL theory.) Therefore, we write the uniform GL free energy as

$$F_{\text{PDW}} = -\alpha \sum_i |\psi_i|^2 + \beta_1 \sum_i |\psi_i|^4 + \beta_2 \sum_{i < j} |\psi_i|^2 |\psi_j|^2 + \beta_3 \sum_{i < j} (\psi_i^{*2} \psi_j^2 + \text{c.c.}), \quad (2)$$

where α and $\beta_{1,2,3}$ are real numbers. Clearly, a large positive β_2 favors nematicity (with unequal $|\psi_i|$), while a positive β_3 causes phase frustration and favors TR breaking. By varying β_2 and β_3 under a fixed value of β_1 , we obtain four possible phases, as shown in Fig. 2(a). Following the usual convention, we use the number of nonzero components to label different PDW phases. In the 1Q phase, only one component is nonzero, which is an extremely nematic PDW. In the 2Q phase, the two nonzero components are found to have the same amplitude but with a relative phase $\pi/2$, which is a chiral 2Q PDW state. The 3Q phases with $|\psi_1| = |\psi_2| = |\psi_3|$ are further divided into two classes: real (up to a global phase) and chiral (with relative phase $2\pi/3$ or $\pi/3$ between each two components). These two types of PDWs can also be denoted as s - and $d \pm id$ wave, respectively, in view of the phase winding along the holo hexagons and the small triangles (detached from the holo hexagons). Both the chiral-2Q and chiral-3Q PDW states break the time reversal symmetry.

Next, let us examine the BdG quasiparticles in these PDW states, by solving the BdG Hamiltonian

$$H = H_0 + \sum_{i, \mathbf{k}, ab} \Delta_i^{ab} c_{a, -\mathbf{k} + \mathbf{Q}_i}^\dagger c_{b, \mathbf{k}}^\dagger + \text{H.c.} \quad (3)$$

where i labels the three M -points, a and b denotes sublattices, and the pairing order parameter Δ_i^{ab} is set according to the eigenvector of the pair susceptibility. For example, for the one shown in Fig. 1(e), it only connects A and B sublattices. A common belief is that the Fermi surface cannot be fully gapped since the pairing electrons with momenta \mathbf{k} and $-\mathbf{k} + \mathbf{Q}$ cannot reside on the FS simultaneously for all momenta [8]. Here, however, we show that this belief is not true for the 3Q PDW states. In Fig. 2(b), we plot the quasiparticle bands in the folded BZ for the chiral 3Q PDW state (the real 3Q state is similar and not shown). The 3Q-PDW opens a full excitation gap, with the gap minimum Δ_m near M_2 . This full gap behavior is a numerical artifact but intrinsic to the 3Q PDW states, which is fundamentally

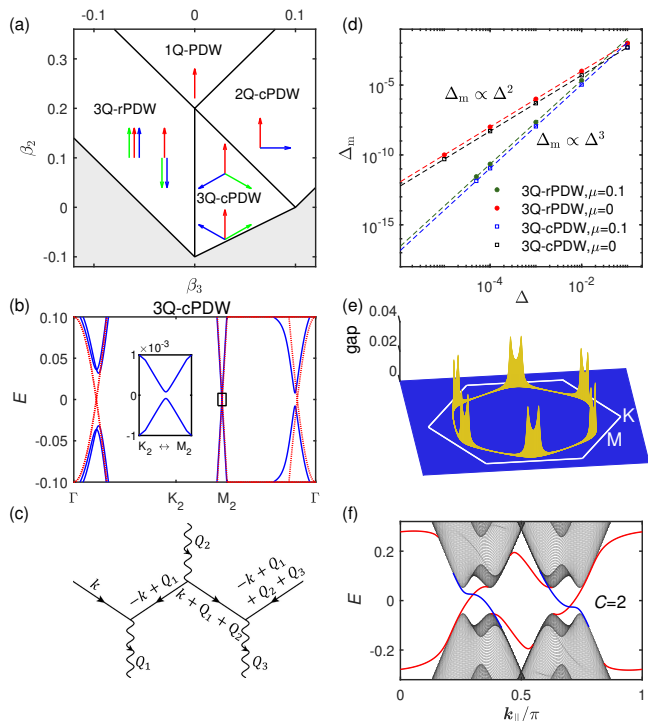


FIG. 2. (a) PDW phase diagram of the GL theory for $\beta_1 = 0.1$. The three colored arrows denote (ψ_1, ψ_2, ψ_3) on the complex plane, up to C_3 -rotations and a global phase. In each 3Q phase, two degenerate patterns are given. The shaded region indicates the absence of a free energy minimum up to fourth order. For these PDW names, “r” means real and “c” means chiral. (b) The low-energy BdG quasiparticle bands in the folded BZ for the chiral 3Q states for $\Delta = |\psi_i| = 0.02$ and $\mu = 0.1$, with the zoom-in near M_2 shown as the inset. For comparison, the normal state bands are given as red dashed lines. (c) Example of the 3rd-order pair scattering diagrams. The solid line denotes fermion and dashed line denotes pairing field ψ (ψ^*) incoming (outgoing) with respect to the three-point vertices. Note that $\mathbf{Q}_{1,2,3} = -\mathbf{Q}_{1,2,3}$ and $\mathbf{Q}_1 + \mathbf{Q}_2 + \mathbf{Q}_3 = 0$ up to reciprocal vectors. (d) The gap minimum Δ_m in the real and chiral 3Q PDW states versus Δ at ($\mu = 0$) or away from ($\mu = 0.1$) the vH filling. (e) The quasiparticle gap near the normal state FS for the chiral 3Q PDW state in (b). (f) The low-energy bands for the chiral 3Q PDW state for $\Delta = 0.4$ on a cylinder with open boundaries along the \mathbf{a}_1 direction, showing two edge states on each boundary (red or blue), consistent with the total Chern number $C = 2$.

different from the 1Q and 2Q states with residual FSs (see Fig. S1 in Supplementary Material [84]). The full gap in the 3Q PDW states can be understood by a higher order degenerate perturbation theory, in which the single particles (described by H_0) are scattered by the pairing terms (in the BdG Hamiltonian Eq. 3), as illustrated in Fig. 2(c): $\mathbf{k} \rightarrow -\mathbf{k} + \mathbf{Q}_1 \rightarrow \mathbf{k} + \mathbf{Q}_1 + \mathbf{Q}_2 \rightarrow -\mathbf{k} + \mathbf{Q}_1 + \mathbf{Q}_2 + \mathbf{Q}_3$. Since $\mathbf{Q}_1 + \mathbf{Q}_2 + \mathbf{Q}_3 = 0$ (up to reciprocal vectors), the third order process always connects $(\mathbf{k}, -\mathbf{k})$ for any \mathbf{k} and thus gaps out the entire FS. In this mechanism, the minimal gap is expected to be proportional to the cube of the order parameter amplitude $\Delta = |\psi_i|$, which is in

good agreement with the numerical results at $\mu = 0.1$ as shown in Fig. 2(d). Note that if the system is exactly at the upper vH filling ($\mu = 0$), the second order process is enough to connect $(\mathbf{k}, \mathbf{k} + \mathbf{Q})$ of equal energy due to the perfect FS nesting. Therefore, the power exponent is reduced from 3 to 2 as seen in Fig. 2(d). For comparison with experiments, we plot the excitation gap near the normal state FS in the unfolded BZ as shown in Fig. 2(e), by calculating the quasiparticle spectral function thereon (see Fig. S2 in Supplementary Material). The \mathbf{k} -dependent excitation gap is maximal (minimal) in the $\Gamma - M$ ($\Gamma - K$) direction. This seems to be consistent with the gap variation on one out of several FSs (in the absence of CDW gap) in a recent ARPES experiment [85] in AV_3Sb_5 up to the resolution uncertainties. In the fully gapped 3Q PDW states, the Chern number C is well defined, which is found to be 0 for the real PDW and ± 2 for the chiral ones. In Fig. 2(f), we show the edge states (two chiral edge modes on each boundary) for the chiral 3Q phase on a cylinder with open boundaries along the \mathbf{a}_1 direction. (Here, a large PDW pairing is assumed to reduce the finite size effect but without loss of the qualitative physics.) It is remarkable that such a topological chiral PDW could emerge from an interacting model without the necessity of spin-orbit coupling. Moreover, the chiral edge states are Weyl fermions, and should exhibit a quantized thermal Hall conductance, $\kappa_{xy}/T = C(\pi^2/3)(k_B^2/h)$ [86], which could be probed in future experiments.

Self-consistent mean field calculations. The above GL analysis indicates four PDW candidate ground states depending on the phenomenological GL parameters $\beta_{1,2,3}$. In this section, we narrow down and sharpen the results by self-consistent mean field calculations with an on-bond pairing interaction

$$H_P = -J \sum_{\langle ij \rangle \sigma \tau} (\sigma c_{i\sigma}^\dagger c_{j\bar{\sigma}}^\dagger) (\tau c_{j\bar{\tau}} c_{i\tau}), \quad (4)$$

where $\langle ij \rangle$ denote the nearest neighbor bonds, $\bar{\sigma} = -\sigma = \pm 1$ and $\bar{\tau} = -\tau = \pm 1$. The total Hamiltonian is $H_0 + H_P$, and the quartic interaction is decoupled in the pairing channel $\sum_{\langle ij \rangle \sigma \tau} -J \langle \sigma c_{i\sigma}^\dagger c_{j\bar{\sigma}}^\dagger \rangle \langle \tau c_{j\bar{\tau}} c_{i\tau} \rangle - J \langle \sigma c_{i\sigma}^\dagger c_{j\bar{\sigma}}^\dagger \rangle \langle \tau c_{j\bar{\tau}} c_{i\tau} \rangle + J \langle \sigma c_{i\sigma}^\dagger c_{j\bar{\sigma}}^\dagger \rangle \langle \tau c_{j\bar{\tau}} c_{i\tau} \rangle$. We require self-consistency in the order parameter $\Delta_{ij} = \sum_{\tau} \tau \langle c_{j\bar{\tau}} c_{i\tau} \rangle$. Here, for simplicity, we do not explicitly distinguish the unitcell and sublattice indices anymore. Since the PDW instability occurs at M , we impose the $2a_0 \times 2a_0$ periodicity on the lattice. After self-consistency is achieved, we also calculate the onsite and on-bond charge densities $n_i = \langle c_{i\sigma}^\dagger c_{i\sigma} \rangle$ and $\chi_{ij} = \langle c_{j\sigma}^\dagger c_{i\sigma} \rangle$, from the latter we obtain the current $\text{Im}(\chi_{ij})$ and valence-bond strength $\text{Re}(\chi_{ij})$.

Our results are summarized in the phase diagram Fig. 3(a). Near the lower vH filling, we find the usual SC with the pairing pattern shown in Fig. 3(b). While near the upper vH filling, we obtain 3Q PDW states only. These results are consistent with the diverging pair susceptibility at Γ (M) near the lower (upper) vH filling.

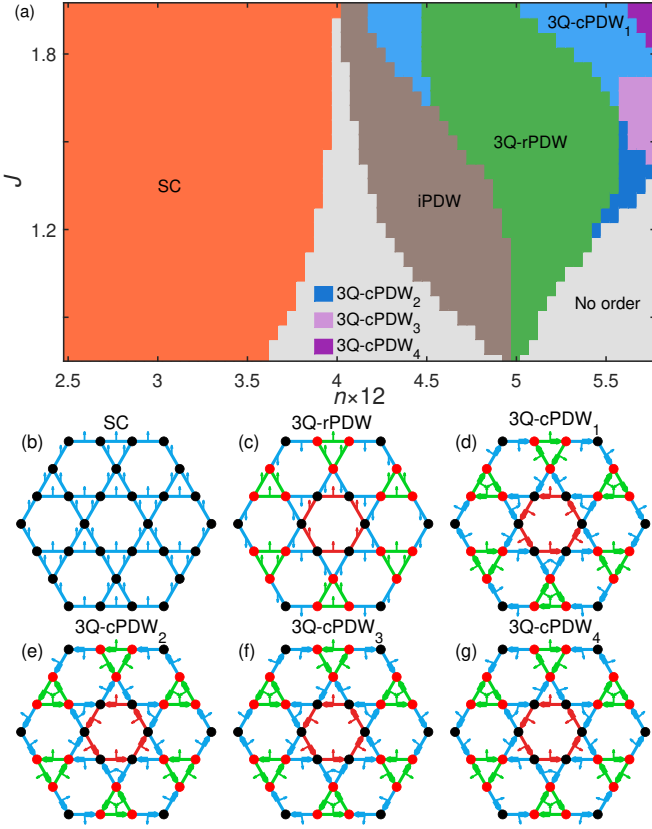


FIG. 3. (a) Mean field phase diagram with respect to on-bond pairing interaction J and filling level n at $T = 0.005$, with different phases represented by different colors. The brown region denotes incommensurate PDW (iPDW). The pairing patterns of different phases are illustrated in (b) to (g) as arrows starting from each bond center. In addition, the induced CDW patterns are also given, with black/red dots denoting n_i , blue/red/green bonds denoting $\text{Re}\chi_{ij}$, and arrows along each bond denoting $\text{Im}\chi_{ij}$.

Larger supercells (up to $6a_0 \times 6a_0$) have been used to check the robustness of these $2a_0 \times 2a_0$ PDW. In the real 3Q PDW phase as shown in Fig. 3(c), one can see that the PDW induces secondary onsite and valence-bond CDWs. The chiral 3Q states are more complicated. It further induces different types of loop current (LC) orders, according to which we further divide it into four subphases as shown in Figs. 3(d-g). For both the real and chiral 3Q PDWs, secondary CDW orders are induced, manifesting intertwining between these two types of orders. The strong intertwining between PDW and other orders has been proposed to explain the variety of competing orders in the pseudogap phase of cuprates [7]. Our study here is clear evidence of the intertwining between PDW and CDW on the kagome lattice based on microscopic calculations. On the other hand, in the brown region below the upper vH filling, we find larger unitcells may further lower the total energy. This is consistent with the fact that the momentum with the largest $\chi(\mathbf{q})$ varies gradually from M to K (not shown) as the filling level

decreases from $\frac{5}{12}$ (upper vH) to $\frac{1}{4}$ (Dirac point). Therefore, we attribute this region as incommensurate PDW.

PDW on CDW: possibility in AV_3Sb_5 . Finally, we examine the possibilities of these PDWs in AV_3Sb_5 , for which the superconductivity occurs inside the CDW state [69–76]. We have seen that the PDWs can induce CDWs. Conversely, the background of CDWs will inevitably affect the PDWs. In AV_3Sb_5 , the microscopic mechanism of (chiral) CDW is still an unsettled issue [87–92]. For our purpose, in order to obtain robust LC (chiral CDW) orders, we adopt the V_1 - V_2 interaction [81]

$$H_V = V_1 \sum_{\langle ij \rangle} n_i n_j + V_2 \sum_{\langle\langle ij \rangle\rangle} n_i n_j, \quad (5)$$

with V_1 (V_2) the (next) nearest neighbor Coulomb repulsion. In the following, the next nearest neighbor hopping $t' = -0.05$ is also included in H_0 to account for the FS revealed by angle-resolved photoemission spectroscopy (ARPES) [93–96]. The pairing interaction term H_P in Eq. 4 is also kept. The total Hamiltonian is $H_0 + H_P + H_V$. In the following mean field calculations, we decouple H_P in the pairing channel, and decouple H_V in the charge bond channel $\sum_{\langle i,j \rangle, \langle\langle ij \rangle\rangle, \sigma} -V_{ij} \langle c_{j\sigma}^\dagger c_{i\sigma} \rangle c_{i\sigma}^\dagger c_{j\sigma} - V_{ij} \langle c_{j\sigma}^\dagger c_{i\sigma} \rangle \langle c_{i\sigma}^\dagger c_{j\sigma} \rangle + V_{ij} \langle c_{j\sigma}^\dagger c_{i\sigma} \rangle \langle c_{i\sigma}^\dagger c_{j\sigma} \rangle$. Exactly speaking, both the quartic H_P and H_V should be decoupled in all possible channels. Here, we just take them as the effective interactions to drive PDW and CDW, respectively.

In Fig. 4, we show two typical mean field solutions. For the first case ($V_1 = 1$, $V_2 = 2$, $J = 1.2$, $n = 0.45$), the temperature dependence of the order parameters are shown in Fig. 4(a), indicating that the PDW can occur inside the CDW state with a lower T_c . Fig. 4(b) shows the ground state with coexisting (almost) real 3Q PDW and chiral CDW. Of course, due to the chiral CDW background, the real 3Q PDW also acquires a weak chirality. This can be understood in the effective GL theory by adding the third-order coupling term

$$\gamma_3 (\psi_1^* \psi_2 \phi_3 + \psi_2^* \psi_3 \phi_1 + \psi_3^* \psi_1 \phi_2 + \text{c.c.}), \quad (6)$$

to F_{PDW} , where ψ_i/ϕ_i are PDW/CDW order parameters and γ_3 is the coupling strength. Clearly, the chiral CDW (complex ϕ_i) drives the chirality of PDW, regardless of the sign of γ_3 . Similarly, Figs. 4(e,f) show the results for the other case ($V_1 = 1.5$, $V_2 = 3$, $J = 1.6$, $n = 0.47$) with the chiral 3Q PDW occurring inside the chiral CDW state. Due to the chiral CDW background, the relative phases between each two PDW components deviate but only slightly from $2\pi/3$. Besides the above 3Q PDW phases, we also obtain a nematic ($\sim 1Q$) PDW phase in the background of nematic CDW (see Fig. S4 in the Supplementary Material [84]), for which a weak chirality is also observed as a result of the intertwining between the two orders. In addition, more results including a phase diagram near the upper vH filling can be found in section III of the Supplementary Material [84].

We see that the PDW can exist at a lower temperature inside the CDW phase due to the intertwining between these two types of orders. This makes it not only

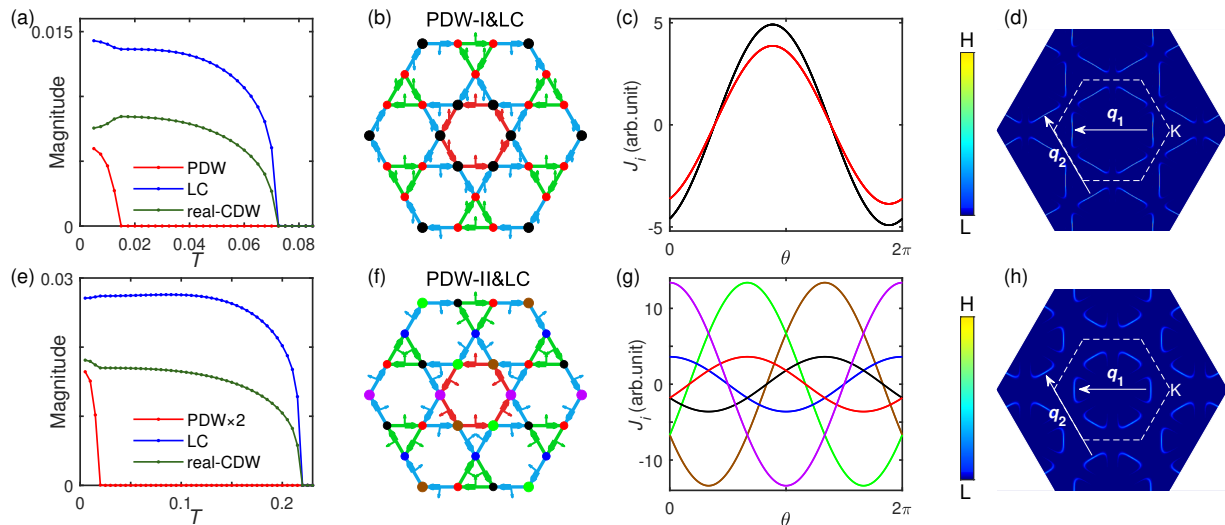


FIG. 4. (a-d) mean field results for $V_1 = 1$, $V_2 = 2$, $J = 1.2$, $n = 0.45$, including temperature-dependence of the order parameters in (a), PDW/CDW patterns in (b), local Josephson currents $J_i(\theta)$ in (c), and unfolded spectral function at zero energy in (d). The pattern convention in (b) is similar to Fig. 3, except the dot size now denotes n_i while the dot color indicates different line-shape of $J_i(\theta)$ in (c). (e-h) are similar plots to (a-d) but for $V_1 = 1.5$, $V_2 = 3$, $J = 1.6$, $n = 0.47$.

of theoretical interest but also a likely candidate for the superconductivity in AV_3Sb_5 . In particular, in a recent experiment [97], some signatures of the $2a_0 \times 2a_0$ PDW have been reported. In view of various experimental progresses, we present some supporting theoretical discussions. (1) We calculate the local Josephson currents $J_i(\theta)$ versus the Josephson phase difference θ (see Sec. I in Supplementary Material [84] for technical details), as shown in Figs. 4(c,g) for the two mean field states, respectively. The critical current $J_{ic} = \max[J_i(\theta)]$, as measured in the scanning Josephson spectroscopy, shows a $2a_0 \times 2a_0$ period, which is consistent with the experiment. (2) The 3Q PDW states are fully gapped but the minimal gap is small, hence, behaving as gapless superconductors with “residual FSs” for realistic experiments with finite energy resolutions. Such a property can be used to distinguish it from the usual SC. As examples, in Figs. 4(d,h), we plot the unfolded single-particle spectral function at zero energy with a realistic scattering rate $\eta = 0.005$, for the two mean field states, respectively. The “residual FSs” provide characteristic scattering vectors \mathbf{q}_1 and \mathbf{q}_2 (up to rotation symmetry), which should be visible in the quasiparticle interference (QPI) pattern (see Fig. S6 in Supplementary Material [84]). We should note, however, that in order to make closer comparison to experiments, one has to take into account the multiple orbitals (or bands) into account, which are beyond our minimal model but deserve further elaborations. (3) The multi-Q (mQ) PDW provides a possibility to support fractional quantum flux $\Phi = \frac{1}{m} \sum_i W_i \Phi_0$ where $\Phi_0 = h/2e$ is the Abrikosov quantum flux and W_i is the winding number of ψ_i . This is a direct generalization of the two-component GL theory for the usual SC [98, 99], and provides an alternative to the charge-4e or -6e pairing to explain the experimentally-

observed half or one-third quantum flux [100].

Summary. We have found robust $2a_0 \times 2a_0$ PDWs on the kagome lattice around the upper vH filling. The properties of these PDWs are studied in GL and mean field theories. By further considering the CDW background, these PDWs are found to be consistent with some of the intriguing superconducting phenomena in AV_3Sb_5 . In particular, our work provide a minimal self-consistent model for the chiral $2a_0 \times 2a_0$ PDW ground state in the kagome lattice with broken time-reversal symmetry and exhibiting topological nontrivial features.

This work is supported by National Key R&D Program of China (Grant No. 2022YFA1403201), National Natural Science Foundation of China (Grant No. 12374147, No. 12274205 and No. 92365203).

Appendix

In this appendix, we first give technical details for the mean field theory, unfolded spectral function, local density of states (LDOS), quasiparticle interference (QPI), and local Josephson current. Then we provide further numerical results referred to but not presented in the main text, in the pure PDW states, and the PDW states on CDW backgrounds. Finally, a microscopic derivation of the GL theory is given.

Appendix A: Technical details

1. Mean field theory

The mean field Hamiltonian with pairing and hopping order parameters on bonds can be written as follows, in

the Nambu basis,

$$H = \sum_{ij} \psi_i^\dagger h_{ij} \psi_j, \quad (\text{A1})$$

where $\psi_i^\dagger = [c_{i\uparrow}^\dagger \ c_{i\downarrow}^\dagger]$ is the Nambu spinor at site i , and h_{ij} is a 2×2 single-particle Hamiltonian

$$h_{ij} = \begin{bmatrix} -t_{ij} - \chi_{ij} - \mu\delta_{ij} & -\Delta_{ij} \\ -\Delta_{ij}^* & t_{ij} + \chi_{ij}^* + \mu\delta_{ij} \end{bmatrix}, \quad (\text{A2})$$

where $t_{ij} = t$ on nearest neighbor (NN) bonds, μ is the chemical potential, $\chi_{ij} = V_{ij} \langle c_{j\sigma}^\dagger c_{i\sigma} \rangle$ (assumed to be independent of the spin σ) is the hopping order parameter on the bond $\langle ij \rangle$, with Coulomb interaction $V_{ij} = V_1$ (V_2) on NN (NNN) bonds, and finally, $\Delta_{ij} = J \langle c_{j\downarrow} c_{i\uparrow} - c_{j\uparrow} c_{i\downarrow} \rangle$ is the singlet pairing order parameter on NN bonds with attractive pairing interaction of strength J . We assume the order parameters are periodic from unitcell to unitcell, and a unitcell contains $m \times m$ primitive cells (so that there are $n = 3m^2$ lattice sites within a unitcell). For the 2×2 PDW and CDW states, we take $m = 2$. (To test whether this is indeed the ground state pattern, we can do the mean field calculations with a larger unitcell, or $m > 2$). In order to take care of the periodicity explicitly, we denote a lattice site as $i = (R, r)$, where R labels the unitcell and r labels the sites within that unitcell, and $R_i = R + r$ is the position vector of this site. We then combine the fields within a unitcell as a spinor

$$\psi_R^\dagger = (c_{\uparrow R,1}^\dagger, c_{\uparrow R,2}^\dagger, \dots, c_{\uparrow R,n}^\dagger, c_{\downarrow R,1}, c_{\downarrow R,2}, \dots, c_{\downarrow R,n}), \quad (\text{A3})$$

by which we can rewrite the Hamiltonian as

$$H = \sum_{R,R'} \Psi_R^\dagger h(R, R') \Psi_{R'} = \sum_k \Psi_k^\dagger h_k \Psi_k, \quad (\text{A4})$$

where h is now an $2n \times 2n$ matrix (which actually depends on $R - R'$ only by the assumed periodicity), whose row (or column) index is composed of (μ, r) , where $\mu = \uparrow, \downarrow$ labels the particle- or hole-part in the Nambu space, and h_k is the Fourier transformation of $h(R, R')$, defined as, by elements,

$$h_k^{\mu r, \mu' r'} = \sum_{R'} h^{\mu r, \mu' r'}(R, R') e^{-ik \cdot (R+r - R'-r')}, \quad (\text{A5})$$

where k is the momentum. Note we include the phase $k \cdot (r - r')$ in the Fourier transformation for later convenience without changing the eigen spectrum (this operation is just a unitary transformation). We define the eigen states of h_k as $h_k |k\ell\rangle = E_{k\ell} |k\ell\rangle$, for $\ell = 1, 2, \dots, 2n$, and denote the particle- and hole-components of the wave function via $|k\ell\rangle = (u_{k\ell}, v_{k\ell})^t$. We calculate the order parameters self-consistently as follows, for $R_i = R + r$ and $R_j = R' + r'$,

$$\chi_{ij} = \frac{V_{ij}}{N_c} \sum_{k\ell} u_{k\ell}^*(r') u_{k\ell}(r) f(E_{k\ell}) e^{ik \cdot (R_j - R_i)}, \quad (\text{A6})$$

$$\Delta_{ij} = \frac{J}{N_c} \sum_{k\ell} [v_{k\ell}^*(r') v_{k\ell}(r) f(E_{k\ell}) e^{ik \cdot (R_j - R_i)} + (R_i \leftrightarrow R_j)], \quad (\text{A7})$$

where N_c is the total number of unitcells on the lattice, $f(E)$ is the Fermi distribution function, and the summation over k is limited within the reduced Brillouin zone (BZ). The local charge density at site $i = (R, r)$ is given by

$$n_i = \frac{1}{N_c} \sum_{k\ell} |u_{k\ell}(r)|^2 f(E_{k\ell}), \quad (\text{A8})$$

where we tune the chemical potential to match the average electron filling.

By the self-consistent mean field calculations, we obtain the results for pure PDW states in Fig. 3, and co-existing PDW/CDW states in Fig. 4 in the main text. Further results will be given in the following.

2. Unfolded spectral function

From the mean field eigenstates, we obtain the Green's function (a $2n \times 2n$ matrix) as a function of momentum at a complex frequency z ,

$$G(k, z) = \sum_i \frac{|k\ell\rangle \langle k\ell|}{z - E_{k\ell}}. \quad (\text{A9})$$

We set $z = i\omega_n$ for Matsubara Green's function at the Matsubara frequency ω_n , and set $z = \omega + i\eta$ for retarded Green's function at real-frequency ω , and η is a smearing factor characteristic of an underlying scattering rate. In this work, unless specified, we use $\eta = 0.005$. A finite smearing factor is always needed to calculate the retarded Green's function. On one hand, the smearing factor may represent the elastic scattering in the real material. On the other hand, a propriate smearing factor is used to reduce the finite-size effect in the calculation. However, we would like to note that if the mini-gap is too small, it may be smeared by smearing factor or elastic scattering within the material.

The unfolded spectral function, which is directly measured by ARPES, can be expressed simply as, for arbitrary momentum k in the unfolded BZ,

$$A(k, \omega) = -\frac{2}{\pi n} \text{Im} \left[\sum_{r,r'} G^{r\uparrow, r'\uparrow}(k, \omega + i\eta) \right], \quad (\text{A10})$$

where the factor of 2 follows from spin summation. For lattices (such as the kagome lattice) with many sites inside a primitive cell, the unfolded spectral function is not necessarily periodic from BZ to extended BZ any more. The spectral weight in the first BZ turns out to be weaker than that in the second BZ. Following the usual convention we plot the stronger spectral function from the second BZ back in the first BZ. Two typical results are shown in Fig. 4(d,h) in the main text.

3. Local density of states and quasiparticle interference

From the mean field eigenstates, we obtain the real-space Green's function (a 2×2 matrix in the Nambu basis),

$$G^{\mu\nu}(i, j; z) = \frac{1}{N_c} \sum_{k\ell} \frac{\langle r\mu|k\ell\rangle \langle k\ell|r'\nu\rangle}{z - E_{k\ell}} e^{ik \cdot (R+r-R'-r')}, \quad (\text{A11})$$

where μ and ν denote the Nambu components, $|r\mu\rangle$ denotes a Nambu-basis state at real-space position r , and $i = (R, r)$ and $j = (R', r')$. The local density of states can be obtained as

$$\rho(i, \omega) = -\frac{2}{\pi} \text{Im} [G^{\uparrow\uparrow}(i, i, \omega)]. \quad (\text{A12})$$

If we add scalar impurity potentials $V_I \tau_3$ (where τ_3 is the Pauli matrix in the Nambu basis) on the lattice sites I (henceforth upper-case letters denote impurity sites), the corrected Green's function at an arbitrary site i (which may or may not be an impurity sites) can be obtained by the T-matrix formalism, dropping the frequency argument for short,

$$\tilde{G}(i, i) = G(i, i) + \sum_{IJ} G(i, I) T_{IJ} G(J, i), \quad (\text{A13})$$

where the summation is over impurity sites, and the T-matrix is given by

$$T_{IJ} = V_I \tau_3 \delta_{IJ} + V_I \tau_3 \sum_{I'} G(I, I') T_{I'J}. \quad (\text{A14})$$

We can use \tilde{G} to obtain the LDOS in the presence of the impurities $\tilde{\rho}(i, \omega)$. The QPI data is the power-spectrum of the modified LDOS $|\tilde{\rho}(q, \omega)|^2$, with $\tilde{\rho}(q, \omega)$ the Fourier transformation of $\tilde{\rho}(i, \omega)$:

$$\tilde{\rho}(q, \omega) = \frac{1}{N} \sum_i \tilde{\rho}(i, \omega) e^{-iq \cdot R_i}. \quad (\text{A15})$$

In our calculations, we place the impurity at the center of a triangle which couples to the densities of the three nearest neighbor sites with equal strength. The resulting LDOS and QPI will be shown and discussed in subsequent sections.

4. Local Josephson current

Suppose a conventional SC lead is connected as a probe in the tunneling limit to the lattice in the form of point-contact. We want to know the Josephson current as a function of the Josephson phase difference, which we define as the phase of the probe θ , setting the overall phase of the PDW as the reference point. The onsite 2×2

Green's function on the probe tip can be well approximated as

$$g(i\omega_n, \theta) \approx -\pi N_0 \frac{i\omega_n \tau_0 + \Delta_0 (\cos \theta \tau_1 - \sin \theta \tau_2)}{\sqrt{\Delta_0^2 + \omega_n^2}}, \quad (\text{A16})$$

where N_0 is the DOS and Δ_0 is the pairing gap in the tip. The local 2×2 Green's function on the lattice site i is just given by $g_i(i\omega_n) = G(i, i, i\omega_n)$, see the previous section. With these ingredients, we can obtain the Josephson current in the tunnelling limit as,

$$J_i(\theta) = -ia^2 T \sum_{\mu, n} \mu g_i^{\bar{\mu}\mu}(i\omega_n) \tilde{g}^{\mu\bar{\mu}}(i\omega_n, \theta) + \text{c.c.}, \quad (\text{A17})$$

where $\mu = 1(\uparrow), -1(\downarrow)$, $\bar{\mu} = -\mu$, and a is the tunneling matrix element. In our calculations, we set $\Delta_0 = 0.01$ and take the temperature $T \rightarrow 0$. Note the Josephson current is not directly measured by STM. Since the working temperature may be well above the Josephson coupling energy, the Josephson tunneling happens in the diffusive regime. Nonetheless, this can lead to a zero-energy-bias peak in the tunneling spectrum, the height of which is proportional to the square of the theoretical Josephson critical current [101]. It is in this sense that STM can probe the Josephson critical current. In the main text, we presented the resulting $J_i(\theta)$ for two representative 3Q PDW states in Fig. 4(c,g). In the subsequent sections, we will present the results for another two cases for comparison and completeness.

Appendix B: Further results for pure PDW phases

In the main text we obtained 3Q-PDW states in the mean field theory, which are most relevant to experiments. However, on general grounds, we also showed that the GL theory allows 1Q- and 2Q-states. Here, for completeness and comparison, we also discuss the properties of the 1Q- and 2Q-PDW states. We plot the quasiparticle bands in the folded BZ for the real and chiral 3Q PDW states, in Fig. 5(a) and Fig. 5(b), respectively. Different from the 3Q PDWs, the 1Q- and 2Q-PDW states are not fully gapped, since not all of the three Q-vectors are present but all of them are required for pair-scattering mechanism illustrated in Fig. 2(c) (main text). Therefore, the 1Q and 2Q PDWs are usual PDW states with genuine residual FSs. To see the residual FSs clearly, the single particle spectral function $A(\mathbf{k}, \omega = 0)$ without unfolding is plotted in Fig. 5(c) for the 1Q-PDW and Fig. 5(d) for the chiral 2Q-PDW.

Corresponding to the four PDW states, the resulting unfolded $A(\mathbf{k}, E = 0)$ are shown in Fig. 5(e-h) accordingly. Although the 3Q PDW states (either real or chiral) are fully gapped, we examined in the main text that the gap minimum is small as it arises from the higher-order pair scattering processes. This might appear as gapless if the gap minimum is within the experimental resolution. We mimic the finite resolution by a scattering rate $\eta = 0.005$ in our calculations. Here, although the

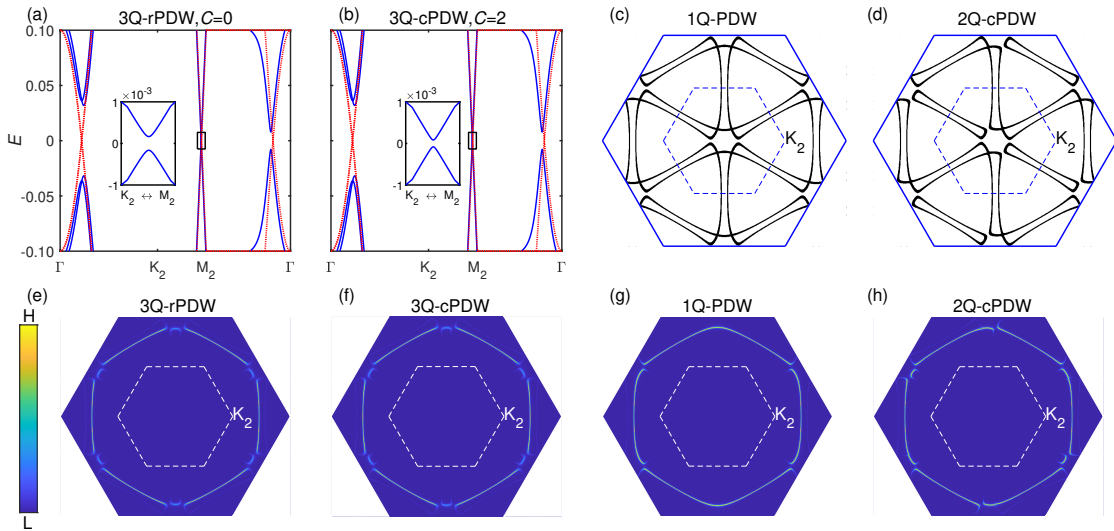


FIG. 5. The low-energy BdG quasiparticle bands for the real and chiral 3Q states are plotted in (a) and (b), respectively, in the folded BZ, with the zoom-in near M_2 shown as the insets. For comparison, the bands without PDW are given as red dashed lines, and the total Chern numbers C of the filled bands are displayed. The FSs for the 1Q and 2Q states are plotted in (c,d). In (e) to (h), the unfolded single-particle spectral functions at zero energy are plotted. In these calculations, we use the BdG parameters $\Delta = 0.02$, $\mu = 0.1$.

“residual FSs” (an artifact from finite scattering rate η) are visible and show similarities to the genuine residual FS in the case of 1Q and 2Q PDWs, the spectral weight distribution around the M -points can still be used to distinguish the 3Q from the nematic 1Q and 2Q PDW states.

In the main text, we presented the quasiparticle gap along the normal state FS. Here, we explain how it is obtained. Due to the finite momentum pairing, the gap does not open exactly on the normal state FS. In other words, the locus of minimal gap along the normal of the FS deviates (but only slightly) from the FS. This can al-

ready be seen in Fig. 5(a,b). This is, in fact, an interesting and also perhaps significant feature to be confirmed by ARPES. Therefore, to obtain the gap minima along the normal direction of the FS, we integrate the unfolded spectral function for each direction over a small k -range near the FS, see the narrow shell enclosing the FS in Fig. 6(a). From the integrated $\bar{A}(\phi, \omega) = \int A(k, \phi, \omega) dk$ shown in Fig. 6(b), we extract the gap size as the bind-

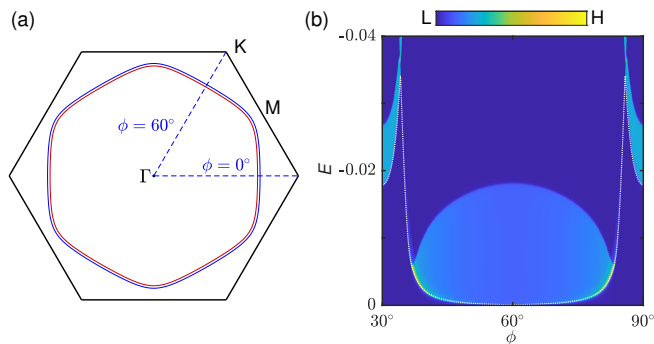


FIG. 6. Around the normal state FS, within the region indicated by the area enclosed by blue (outside the FS) and red (inside the FS) lines in (a), we calculate the integrated spectral function $\bar{A}(\phi, \omega)$ in the 3Q-cPDW state as shown in (b). The white dotted line represents the resulting quasiparticle gap. In the calculations, we use the parameters $\Delta = 0.02$, $\mu = 0.1$, $\eta = 0.0001$.

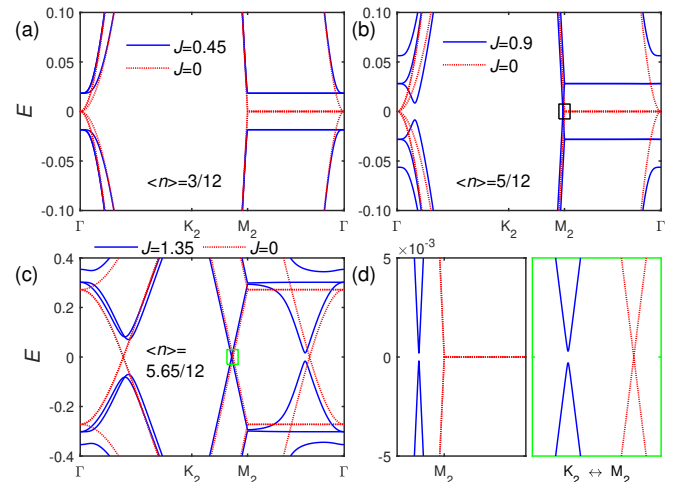


FIG. 7. Low-energy BdG quasiparticle bands along the high-symmetry path in the reduced BZ obtained by mean field calculations. Red dashed lines corresponding to normal state at $J = 0$ are plotted for comparison. (d) Zoom-in of low-energy band dispersions inside black and green boxes in (b) and (c), respectively.

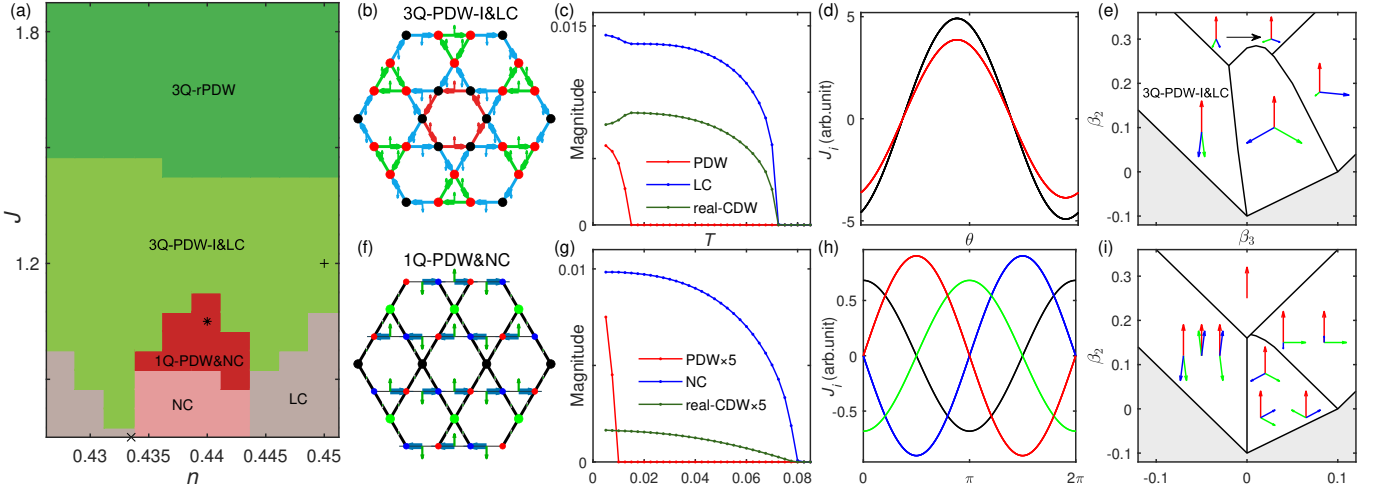


FIG. 8. (a) Mean field phase diagram around the upper vH filling (marked by \times) for $V_1 = 1$, $V_2 = 2$, $t' = -0.05$ and $T = 0.005$. For the representative case marked by $+$, the PDW and CDW patterns are plotted in (b) with the same convention in Fig. 3 in the main text, the temperature dependence of the order parameters are plotted in (c), and the local Josephson current J_i versus the pairing phase θ are plotted in (d) with the line colors corresponding to different sites in (b). Under this LC background, the GL phase diagram is shown in (e) with the same convention as Fig. 2(a) in the main text, for $\alpha = 1$, $\beta_1 = 0.1$, $\gamma_1 = -2\beta_1$, and $\gamma_2 = \gamma_3 = \beta_1$. For the other representative case marked by $*$, the results are similarly plotted in (f) to (i).

ing energy on the lower edge of the excitation spectrum for each direction. The resulting gap along the FS are plotted in Fig. 2(e) in the main text.

The BdG quasiparticle bands, obtained by self-consistent mean-field calculations, are shown in Fig. 7. For the usual SC state at the lower vH filling, see Fig. 7(a), the BdG quasiparticle bands open uniform energy gaps at the Fermi energy. While for the 3Q-rPDW state [see Fig. 7(b)], and 3Q-cPDW [see Fig. 7(c)], the gaps do not uniformly open along the high symmetry path and leaves a minigap near point M_2 . Fig. 7(d) is the Zoom-in of band dispersions inside black and green boxes in Fig. 7(b,c), demonstrating the small but finite gap minimum.

Appendix C: Further results for PDW on CDW backgrounds

By self-consistent mean field calculations, we obtain the phase diagram near the upper vH filling for $V_1 = 1$, $V_2 = 2$, $t' = -0.05$ and $T = 0.005$ as shown in Fig. 8(a). We observe that in the majority of the given parameter space the 3Q-PDW states are realized. For completeness and comparison, here we also discuss the other phases. At small J , two types of CDW orders are obtained: the loop current (LC) [see Fig. 8(b)] and nematic current (NC) [see Fig. 8(f)] orders. As J increases, the 3Q PDW-I (almost real 3Q PDW) is formed on the LC state [see Fig. 8(b)] but with a lower T_c [see Fig. 8(c)]. On the other hand, in the NC state, increasing J firstly induces the 1Q PDW order [see Fig. 8(f), the current and PDW orders on other bonds are very small] also with a lower T_c [see Fig. 8(g)], and then the 3Q PDW-I occurs and coexists

with the LC order. For sufficiently large J , the LC order vanishes and only the 3Q real PDW (with secondary real CDW) is left. For the above two representative cases, the local Josephson currents $J_i(\theta)$ are plotted in Fig. 8(d) and (h), respectively. Clearly, the critical current shows $a_0 \times a_0$ periodicity in the nematic 1Q (same for 2Q, not shown) PDW state, but $2a_0 \times 2a_0$ periodicity in the real 3Q (same for chiral 3Q, already shown in the main text) PDW state.

To gain qualitative insights into the interplay between PDW and CDW, we resort to GL theory in a given CDW background. We add symmetry-allowed couplings between the PDW ψ_i and CDW order parameters ϕ_i to F_{PDW} as

$$F = F_{\text{PDW}} + \gamma_1 \sum_i |\psi_i|^2 |\phi_i|^2 + \gamma_2 \sum_{i < j} |\psi_i|^2 |\phi_j|^2 + \gamma_3 (\psi_1^* \psi_2 \phi_3 + \psi_2^* \psi_3 \phi_1 + \psi_3^* \psi_1 \phi_2 + \text{c.c.}) \quad (\text{C1})$$

where $\gamma_{1,2,3}$ are real numbers. For a given CDW $\phi_{1,2,3}$ and the couplings $\gamma_{1,2,3}$, we can find all possible PDW ground states. As an illustration, we choose $\gamma_1 = -2\beta_1$ and $\gamma_2 = \gamma_3 = \beta_1$. (Here, to compare with the mean field results, we set $\gamma_1 < 0$ and $\gamma_2 > 0$ to realize the 1Q PDW on the 1Q nematic CDW state, and set $\gamma_3 > 0$ to realize the real 3Q PDW on the 3Q LC state.) For the chiral CDW, we set $\phi_1 = \phi_2 = \phi_3 = e^{i\alpha}$ ($\alpha \approx 0.7\pi$) as obtained from mean field calculations. The phase diagram is shown in Fig. 8(e). We can identify the above two mean field ground states as inheriting from the real and chiral 3Q PDWs, respectively, by comparing with Fig. 2(a) in the main text. Due to the chiral CDW background, the chiral 3Q PDW phase (PDW-II) is enlarged, and the real 3Q PDW state (PDW-I) acquires a weak chirality as a result of the γ_3 -term, consistent with our mean field result

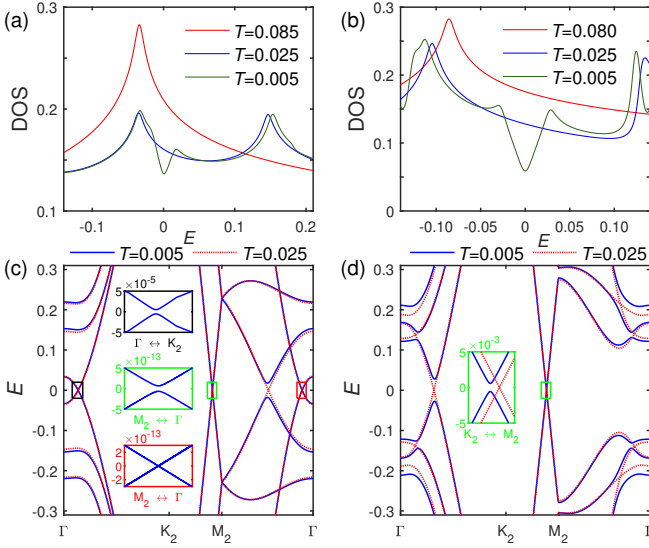


FIG. 9. For $J = 1.05$, $n = 0.44$ marked by * in Fig. 8(a), (a) shows the DOS at different temperatures. (c) displays the low-energy BdG quasiparticle bands along one of three non-equivalent $\Gamma - K_2 - M_2 - \Gamma$, with insets zooming in on band dispersions. (b) and (d) is similar to (a) and (c), respectively, but for $J = 1.2$, $n = 0.45$ marked by + in Fig. 8(a).

in Fig. 8(b). In addition, there are another two nematic phases inheriting from the 1Q and 2Q PDWs. The former is realized on a nematic CDW background, while the latter may be realized in other microscopic models.

We further study the 1Q-PDW&NC and 3Q-PDW-I&LC phases in Fig. 8(a). Fig. 9(a,b) show the DOS $\rho(E)$ at different temperatures for two sets of values of J and n , which correspond to the two representative states marked by * and + in Fig. 8(a). The DOS exhibits a CDW gap at $T = 0.025$ compared to the normal state. Furthermore, at $T = 0.005$, a V-shaped superconducting gap opens in the CDW state, which corresponds to the gapless BdG quasiparticle bands for 1Q-PDW&NC and to the quasiparticle bands with a very small gap for 3Q-PDW-I&LC as shown in Fig. 9(c,d). It is worth noting that the V-shaped superconducting gap has been observed in several experiments [25, 102–105] in kagome superconductors.

In the main text, we presented the “residual FSs” for the 3Q PDWs. Here, we provide further results in the pure-CDW state and the QPI spectrum. Fig. 10 shows the unfolded spectral functions $A(\mathbf{k}, E)$ and the QPI at the Fermi energy for the two representative states marked by * and + in Fig. 8(a). In the CDW states, two bar-like signals are observed at \mathbf{q}_1 and \mathbf{q}_2 in Fig. 10(e,g). As the temperature decreases, PDWs emerge, but the bar-like signals persist at \mathbf{q}_1 and \mathbf{q}_2 , as depicted in Fig. 10(f,h). The persistence of such features in the SC state serves as an indicator of the “residual FS” in the PDW state.

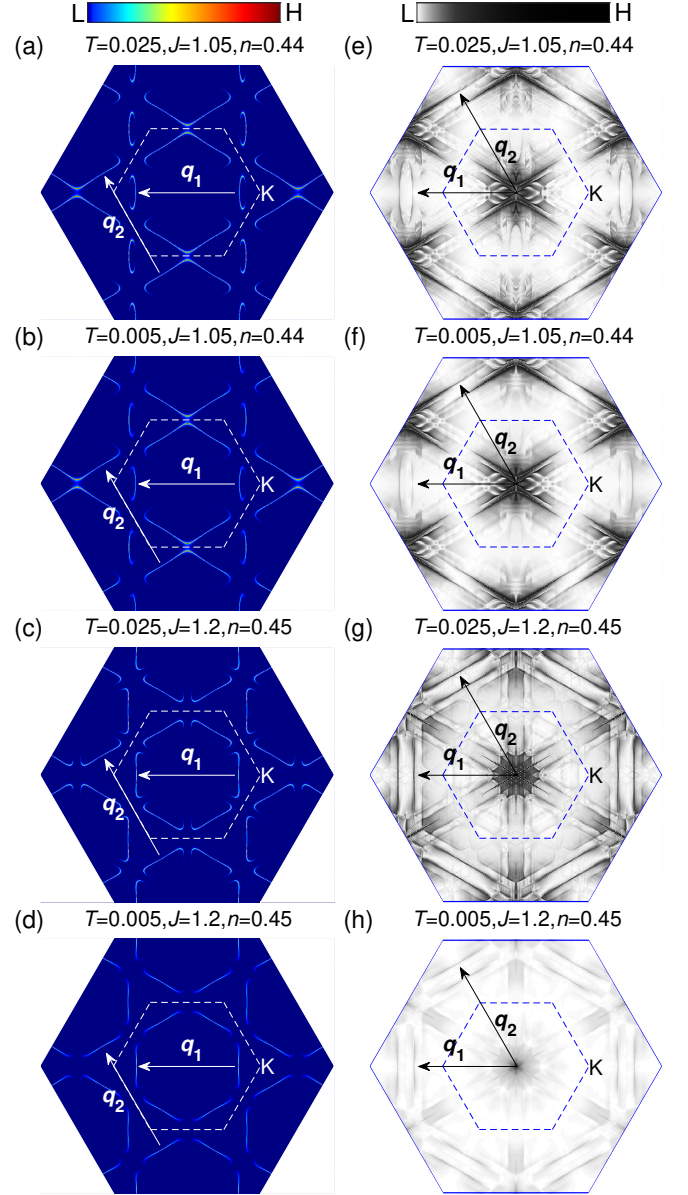


FIG. 10. The unfolded spectral functions $A(\mathbf{k}, E = 0)$ at two temperatures are plotted in (a,b) for the state marked by * in Fig. 8(a), and (c,d) for the state marked by +, respectively. (e-h) QPI maps at Fermi energy corresponding to (a-d).

Appendix D: LDOS of PDW orders

In particular, we focus on LDOS in different cases.

1. The LDOS of PDW and CDW-PDW state

First, we only consider PDW state. We set $\chi_{ij} = 0$ and $\Delta_{ij} = |\Delta_{ij}| \exp(i\phi_{ij})$, which are shown in Fig. 11(a). The length and direction of the arrows denote magnitude $|\Delta_{ij}| = 0.02$ and phase ϕ_{ij} , respectively. As shown in Fig. 12, the corresponding LDOS on sites A and B

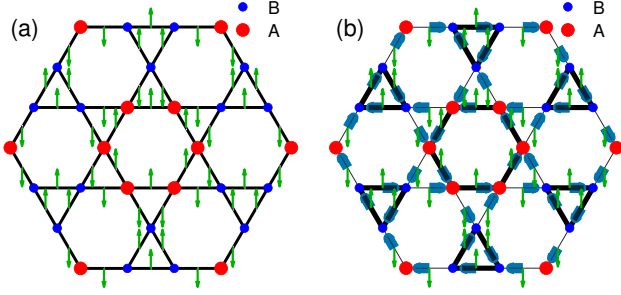


FIG. 11. Schematics of the $2a_0 \times 2a_0$ state. The size of the circle on the site denotes particle number $\langle n_i \rangle$, the thickness of bonds denote the real CDW order parameters $t - \text{Re}(\chi_{ij})$, arrows starting from the middle of bonds indicate the PDW order parameters Δ_{ij} and arrows on the bonds indicate the imaginary CDW order parameters $\text{Imag}(\chi_{ij})$.

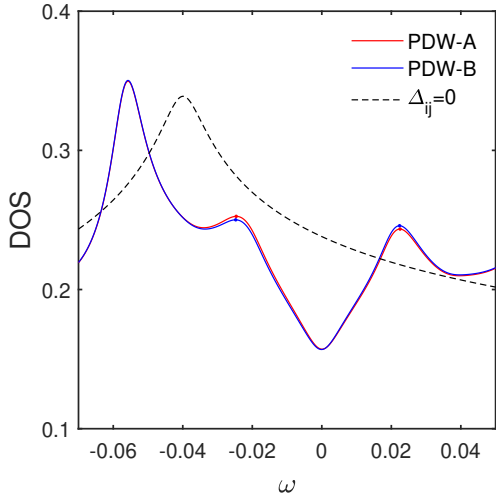


FIG. 12. The LDOS for $\chi_{ij} = 0$, $|\Delta_{ij}| = 0.02$ and $\mu = 0.04$. Dots denote local maxima.

show small differences around superconducting coherence peaks.

Experimentally, CDW and PDW are co-existing at low temperatures and the superconducting gap is smaller than CDW gap, so we consider $|\text{Re}(\chi_{ij})| = 0.1$, $|\text{Imag}(\chi_{ij})| = 0.1$ and $|\Delta_{ij}| = 0.01$. As shown in Fig. 11(b), the thick (thin) bonds denote $\text{Re}(\chi_{ij}) = -0.1(0.1)$ and the direction of arrows on the bonds denotes the flowing direction of imaginary CDW (loop current) order.

Fig. 13 shows the LDOS on sites A and B, the superconducting coherence peaks are around $\omega = \pm 0.015$ and the difference between A and B is small.

2. The LDOS of Nematic-PDW and CDW-Nematic-PDW state

Experimentally, PDW may be nematic. We consider the Nematic-PDW (NPDW) as Fig. 14(a), $\chi_{ij} = 0$,

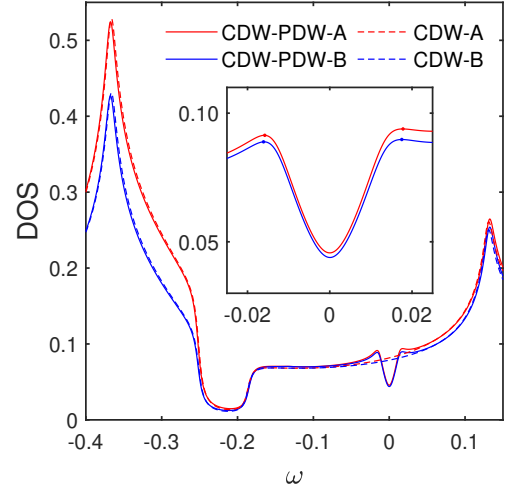


FIG. 13. The LDOS for $|\text{Re}(\chi_{ij})| = 0.1$, $|\text{Imag}(\chi_{ij})| = 0.1$, $|\Delta_{ij}| = 0.01$ ($|\text{Re}(\chi_{ij})| = 0.1$, $|\text{Imag}(\chi_{ij})| = 0.1$, $|\Delta_{ij}| = 0$) and $\mu = 0.04$ are represented by solid (dashed) lines. The inset shows the zoom-in of LDOS around the superconducting coherence peaks and dots denote local maxima.

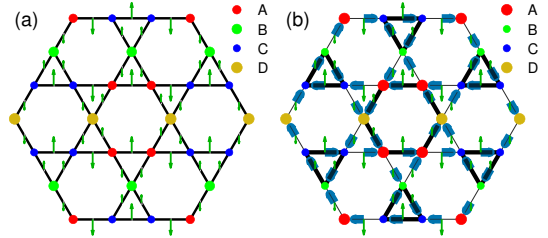


FIG. 14. Schematics of the $2a_0 \times 2a_0$ state. The size of the circle on the site denotes particle number $\langle n_i \rangle$, the thickness of bonds denote the real CDW order parameters $t - \text{Re}(\chi_{ij})$, arrows starting from the middle of bonds indicate the PDW order parameters Δ_{ij} and arrows on the bonds indicate the imaginary CDW order parameters $\text{Imag}(\chi_{ij})$.

$|\Delta_{ij}|_{\text{max}} = 0.04$ and $|\Delta_{ij}|_{\text{min}} = 0.024$. The corresponding LDOS on sites A, B, C and D are shown in Fig. 15, and the difference between the locations of local maxima for different sites is larger than that in Fig. 12.

For CDW and Nematic-PDW coexisting, as shown in Fig. 14(b), we set $|\text{Re}(\chi_{ij})| = 0.1$, $|\text{Imag}(\chi_{ij})| = 0.1$, $|\Delta_{ij}|_{\text{max}} = 0.02$, $|\Delta_{ij}|_{\text{min}} = 0.012$. Fig. 16 shows the LDOS on different sites, there are obvious changes in the locations of local maxima as the sites shift.

Appendix E: Microscopic derivation of the Ginzburg-Landau theory

We first consider H_P , as given in Eq. (4) of the main text, the path integral representation of the partition

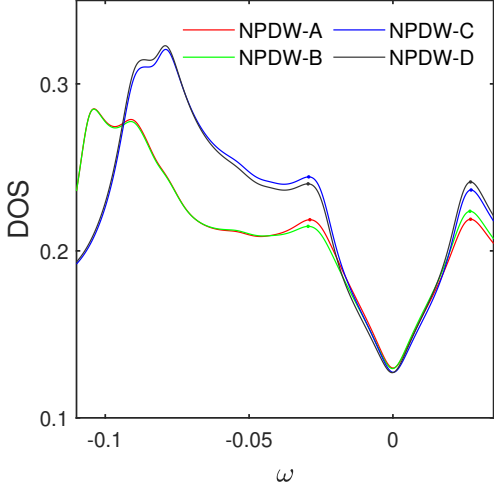


FIG. 15. The LDOS for $\chi_{ij} = 0$, $|\Delta_{ij}|_{\max} = 0.04$, $|\Delta_{ij}|_{\min} = 0.024$ and $\mu = 0.07$. Dots denote local maxima.

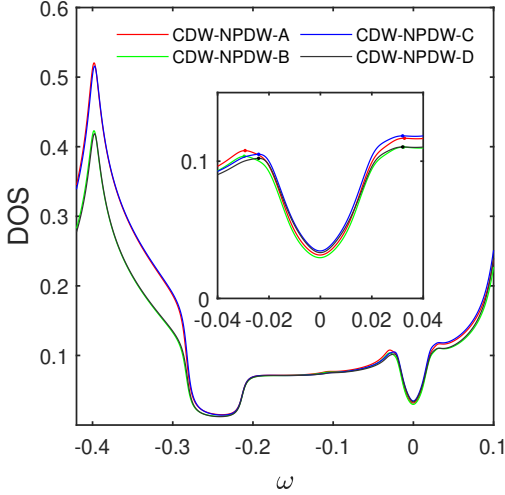


FIG. 16. The LDOS for $|\text{Re}(\chi_{ij})| = 0.1$, $|\text{Imag}(\chi_{ij})| = 0.1$, $|\Delta_{ij}|_{\max} = 0.02$, $|\Delta_{ij}|_{\min} = 0.012$ and $\mu = 0.07$. The inset shows the zoom-in of LDOS around the superconducting coherence peaks and dots denote local maxima.

function is

$$Z = \int D\bar{\varphi}D\varphi e^{-S}; \quad S = S_0 + S_I \quad (\text{E1})$$

$$S_0 = \int_0^{\frac{1}{T}} d\tau \sum_{i\sigma} \bar{\varphi}_{i\sigma} (\partial_\tau - \mu) \varphi_{i\sigma} - \sum_{ij\sigma} (t_{ij} \bar{\varphi}_{i\sigma} \varphi_{j\sigma} + \text{H.c.}) \quad (\text{E2})$$

$$S_I = \int_0^{\frac{1}{T}} d\tau (-J) \sum_{\langle ij \rangle} (\bar{\varphi}_{i\uparrow} \bar{\varphi}_{j\downarrow} - \bar{\varphi}_{i\downarrow} \bar{\varphi}_{j\uparrow}) (\varphi_{j\downarrow} \varphi_{i\uparrow} - \varphi_{j\uparrow} \varphi_{i\downarrow}) \quad (\text{E3})$$

By Hubbard-Stratonovich decomposition to introduce

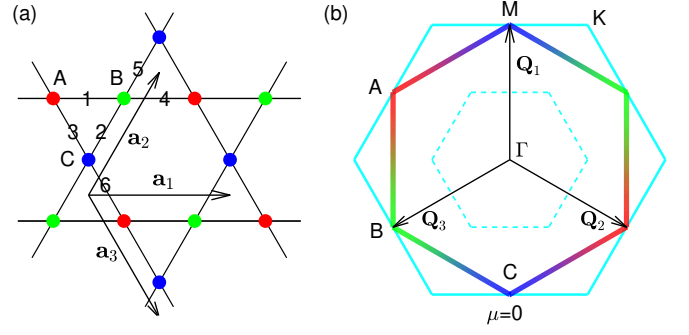


FIG. 17. (a) Kagome lattice structure with the three sublattices labeled by A (red), B (green) and C (blue), respectively. $\mathbf{a}_{1,2,3}$ denote three translation vectors with length a_0 . The numbers 1 to 6 represent the six bonds within a unit cell. (b) The three vectors $\mathbf{Q}_{b=1,2,3}$ are depicted in the first BZ, the color-scaled line represents the FS at the upper vH filling.

the pairing field, we obtain

$$Z = \int D\bar{\varphi}D\varphi \int D\bar{\psi}D\psi e^{-S} \quad (\text{E4})$$

$$S = \int_0^{\frac{1}{T}} d\tau \sum_{i\sigma} \bar{\varphi}_{i\sigma} (\partial_\tau - \mu) \varphi_{i\sigma} - \sum_{ij\sigma} (t_{ij} \bar{\varphi}_{i\sigma} \varphi_{j\sigma} + \text{H.c.})$$

$$+ \sum_{R,\tilde{b}} (-[\psi_{R,\tilde{b}}^\dagger \sum_{\alpha_{\tilde{b}}} \bar{\varphi}_{R+\delta(\alpha_{\tilde{b}}),\uparrow} \bar{\varphi}_{R+\delta(\bar{\alpha}_{\tilde{b}}),\downarrow} + \text{H.c.}] + \frac{1}{J} |\psi_{R,\tilde{b}}|^2) \quad (\text{E5})$$

where R labels the unitcell, $\tilde{b} = 1, 2, \dots, 6$ specifies the bond within an unitcell, as shown in Fig. 17(a), and $(\alpha_{\tilde{b}}, \bar{\alpha}_{\tilde{b}})$ correspond to the sublattice indices at the two ends of bond \tilde{b} . For instance, when $\tilde{b} = 1$, $\alpha_{\tilde{b}}(\bar{\alpha}_{\tilde{b}}) = A(B), B(A)$. $\psi_{R,\tilde{b}}$ represents the bosonic auxiliary pairing field located on bond \tilde{b} within the unit cell R . $\delta(\alpha_{\tilde{b}})$ represents the offset between the unit cell containing the endpoint $\alpha(\tilde{b})$ of bond \tilde{b} and the unit cell R . For example, when $\tilde{b} = 2$, $\delta(A_2) = \mathbf{a}_1$ and $\delta(B_2) = 0$.

We now introduce the Fourier transformation

$$\varphi_{\mathbf{R},\tau}^\alpha = \sqrt{\frac{T}{N}} \sum_{\mathbf{k},\omega_n} e^{-i\omega_n\tau + i\mathbf{k}\cdot\mathbf{R}} \varphi_{\mathbf{k},\omega_n}^\alpha \quad (\text{E6})$$

$$\psi_{\mathbf{R},\tau}^{\tilde{b}} = \sum_{\mathbf{q},\nu_n} e^{-i\nu_n\tau + i\mathbf{q}\cdot\mathbf{R}} \psi_{\mathbf{q},\nu_n}^{\tilde{b}} \quad (\text{E7})$$

and obtain:

$$S = \sum_{k,\sigma} \sum_{\alpha\beta} \bar{\varphi}_{k,\sigma}^\alpha (-i\omega_n \delta_{\alpha\beta} + h_{\mathbf{k}}^{\alpha\beta}) \varphi_{k,\sigma}^\beta + \sum_{q,b} \frac{N}{JT} |\psi_q^{\tilde{b}}|^2 +$$

$$\sum_{k,q,\tilde{b}} -[\psi_q^{\tilde{b}} \sum_{\alpha_{\tilde{b}}} \bar{\varphi}_{k,\uparrow}^{\alpha_{\tilde{b}}} \bar{\varphi}_{-k+q,\downarrow}^{\bar{\alpha}_{\tilde{b}}} e^{-i(\mathbf{k}\cdot\delta(\alpha_{\tilde{b}}) + [-\mathbf{k}+\mathbf{q}]\cdot\delta(\bar{\alpha}_{\tilde{b}}))} + \text{H.c.}] \quad (\text{E8})$$

where $k = (\mathbf{k}, \omega_n)$, $q = (\mathbf{q}, \nu_n)$, and $\alpha, \beta = A, B, C$. We will neglect the temporal fluctuation of ψ . Following the discussion in the main text, we simplify our notation with

$\psi_{\bar{b}} = \psi_{q=\pm Q_{\bar{b}}}^{\bar{b}}$, where $Q_{\bar{b}} = (\mathbf{Q}_{\bar{b}}, \nu_n = 0)$, with $Q_4 = Q_1, Q_5 = Q_2, Q_6 = Q_3$, and $\psi_4 = -\psi_1, \psi_5 = -\psi_2, \psi_6 = -\psi_3$. The vectors $\mathbf{Q}_{b=1,2,3}$ are illustrated in Fig. 17(b). Next, we turn to the Nambu spinor representation $\bar{\varphi} = (\bar{\varphi}_{\uparrow}, \varphi_{\downarrow})$, where φ_{σ} list all k and α . The effective action is then given by

$$S = \frac{2N}{JT} (|\psi_1|^2 + |\psi_2|^2 + |\psi_3|^2) - \bar{\varphi}(\mathcal{G}_0^{-1} + \Delta)\varphi \quad (\text{E9})$$

where \mathcal{G}_0 is the Gor'kov function in Nambu space. It is related to the normal state single particle function G_0 as follows

$$[\mathcal{G}_{0,\uparrow\uparrow}]_k^{\alpha\beta} = [(\mathrm{i}\omega_n - \tilde{h}_{\mathbf{k}})^{-1}]^{\alpha\beta} \equiv G_{0,k}^{\alpha\beta} \quad (\text{E10})$$

$$\begin{aligned} [\mathcal{G}_{0,\downarrow\downarrow}]_{-k}^{\alpha\beta} &= [(\mathrm{i}\omega_n + \tilde{h}_{-\mathbf{k}}^T)^{-1}]^{\alpha\beta} \\ &= -[(\mathrm{i}(-\omega_n) - \tilde{h}_{-\mathbf{k}})^{-1}]^{\beta\alpha} \equiv -G_{0,-k}^{\beta\alpha} \end{aligned}$$

Δ is the pairing matrix, and it satisfies the following relations

$$\Delta_{k_{\uparrow}, -k \pm Q_{b\downarrow}}^{\alpha_b, \bar{\alpha}_b} = \psi_b \cdot f_{\Delta}(k, \alpha_b; -k \pm Q_b, \bar{\alpha}_b) \quad (\text{E11})$$

$$\Delta_{-k \pm Q_{b\downarrow}, k_{\uparrow}}^{\bar{\alpha}_b, \alpha_b} = \psi_b^* \cdot f_{\Delta}^*(k, \alpha_b; -k \pm Q_b, \bar{\alpha}_b) \quad (\text{E12})$$

$$\begin{aligned} f_{\Delta}(k, \alpha_b; -k \pm Q_b, \bar{\alpha}_b) &\equiv e^{-\mathrm{i}(\mathbf{k} \cdot \boldsymbol{\delta}(\alpha_b) + [-\mathbf{k} + \mathbf{Q}_b] \cdot \boldsymbol{\delta}(\bar{\alpha}_b))} \\ &\quad - e^{-\mathrm{i}(\mathbf{k} \cdot \boldsymbol{\delta}(\alpha_{b+3}) + [-\mathbf{k} + \mathbf{Q}_b] \cdot \boldsymbol{\delta}(\bar{\alpha}_{b+3}))} \end{aligned} \quad (\text{E13})$$

$$f_{\Delta}(k, \alpha_b; -k \pm Q_b, \bar{\alpha}_b) = f_{\Delta}(-k \pm Q_b, \bar{\alpha}_b; k, \alpha_b) \quad (\text{E14})$$

$$f_{\Delta}(k, \alpha_b; -k + Q_b, \bar{\alpha}_b) = f_{\Delta}(k, \alpha_b; -k - Q_b, \bar{\alpha}_b) \quad (\text{E15})$$

where $b = 1, 2, 3$.

The path integral can be completed exactly, giving us

the GL free energy

$$F = -\frac{T \ln Z}{N} = \frac{2}{J} (|\psi_1|^2 + |\psi_2|^2 + |\psi_3|^2) - \frac{T}{N} \text{Trln}(\mathcal{G}_0^{-1} + \Delta) \quad (\text{E16})$$

The order parameters $\psi_{b=1,2,3}$ are needed to be optimized to minimize F . Our task thus reduced to computing the expansion of $\text{Trln}(\mathcal{G}_0^{-1} + \Delta)$

$$\begin{aligned} \text{Trln}(\mathcal{G}_0^{-1} + \Delta) &= \text{Trln}(\mathcal{G}_0^{-1} [1 + \mathcal{G}_0 \Delta]) \\ &= \text{Trln}(\mathcal{G}_0^{-1}) + \text{Trln}(1 + \mathcal{G}_0 \Delta) \\ &= \text{const.} - \sum_{n=\text{even}}^{\infty} \frac{1}{n} \text{Tr}(\mathcal{G}_0 \Delta)^n \end{aligned} \quad (\text{E17})$$

Note that $[\mathcal{G}_0 \Delta]$ is off-diagonal in Nambu space, only even orders are nonzero after the trace operation.

The second-order term is

$$\begin{aligned} -\frac{1}{2} \text{Tr}(\mathcal{G}_0 \Delta)^2 &= -\text{Tr}([\mathcal{G}_{0,\uparrow\uparrow}] \Delta_{\uparrow\downarrow} [\mathcal{G}_{0,\downarrow\downarrow}] \Delta_{\downarrow\uparrow}) \\ &= - \sum_{b=1,2,3} \sum_{\alpha_b, \beta_b} \sum_k \\ &\quad [\mathcal{G}_{0,\uparrow\uparrow}]_k^{\beta_b, \alpha_b} \Delta_{k_{\uparrow}, -k + Q_{b\downarrow}}^{\alpha_b, \bar{\alpha}_b} [\mathcal{G}_{0,\downarrow\downarrow}]_{-k + Q_b}^{\bar{\alpha}_b, \beta_b} \Delta_{-k + Q_{b\downarrow}, k_{\uparrow}}^{\beta_b, \bar{\beta}_b} \end{aligned} \quad (\text{E18})$$

$$\begin{aligned} &= \sum_b |\psi_b|^2 \sum_{\alpha_b, \beta_b} \sum_k [G_{0,k}^{\bar{\beta}_b, \alpha_b} G_{0,-k+Q_b}^{\beta_b, \bar{\alpha}_b} \\ &\quad \cdot f_{\Delta}(k, \alpha_b; -k + Q_b, \bar{\alpha}_b) f_{\Delta}^*(k, \bar{\beta}_b; -k + Q_b, \beta_b)] \end{aligned} \quad (\text{E19})$$

The corresponding Feynman diagram is shown in Fig. 18(a).

The fourth-order term is

$$\begin{aligned} -\frac{1}{4} \text{Tr}(\mathcal{G}_0 \Delta)^4 &= -\frac{1}{2} \text{Tr}([\mathcal{G}_{0,\uparrow\uparrow}] \Delta_{\uparrow\downarrow} [\mathcal{G}_{0,\downarrow\downarrow}] \Delta_{\downarrow\uparrow} [\mathcal{G}_{0,\uparrow\uparrow}] \Delta_{\uparrow\downarrow} [\mathcal{G}_{0,\downarrow\downarrow}] \Delta_{\downarrow\uparrow}) \\ &= -\frac{1}{2} \sum_{b_1, b_2, b_3, b_4} \sum_{\alpha_{b_1}, \beta_{b_2}, \gamma_{b_3}, \eta_{b_4}} \sum_k [\mathcal{G}_{0,\uparrow\uparrow}]_k^{\eta_{b_4}, \alpha_{b_1}} \Delta_{k_{\uparrow}, -k + Q_{b_1\downarrow}}^{\alpha_{b_1}, \bar{\alpha}_{b_1}} [\mathcal{G}_{0,\downarrow\downarrow}]_{-k + Q_{b_1}}^{\bar{\alpha}_{b_1}, \beta_{b_2}} \Delta_{-k + Q_{b_1\downarrow}, k - Q_{b_1} + Q_{b_2\uparrow}}^{\beta_{b_2}, \bar{\beta}_{b_2}} \\ &\quad \cdot [\mathcal{G}_{0,\uparrow\uparrow}]_{k - Q_{b_1} + Q_{b_2}}^{\bar{\beta}_{b_2}, \gamma_{b_3}} \Delta_{k - Q_{b_1} + Q_{b_2\uparrow}, -k + Q_{b_1} - Q_{b_2} + Q_{b_3\downarrow}}^{\gamma_{b_3}, \bar{\gamma}_{b_3}} [\mathcal{G}_{0,\downarrow\downarrow}]_{-k + Q_{b_1} - Q_{b_2} + Q_{b_3}}^{\bar{\gamma}_{b_3}, \eta_{b_4}} \Delta_{-k + Q_{b_1} - Q_{b_2} + Q_{b_3\downarrow}, k_{\uparrow}}^{\eta_{b_4}, \bar{\eta}_{b_4}} \end{aligned} \quad (\text{E20})$$

$$\begin{aligned} &= -\frac{1}{2} \sum_{b_1, b_2, b_3, b_4} \psi_{b_1} \psi_{b_2}^* \psi_{b_3} \psi_{b_4}^* \sum_{\alpha_{b_1}, \beta_{b_2}, \gamma_{b_3}, \eta_{b_4}} \sum_k G_{0,k}^{\bar{\eta}_{b_4}, \alpha_{b_1}} G_{0,-k+Q_{b_1}}^{\beta_{b_2}, \bar{\alpha}_{b_1}} G_{0,k-Q_{b_1}+Q_{b_2}}^{\bar{\beta}_{b_2}, \gamma_{b_3}} G_{0,-k+Q_{b_1}-Q_{b_2}+Q_{b_3}}^{\eta_{b_4}, \bar{\gamma}_{b_3}} \\ &\quad \cdot f_{\Delta}(k, \alpha_{b_1}; -k + Q_{b_1}, \bar{\alpha}_{b_1}) \cdot f_{\Delta}^*(k - Q_{b_1} + Q_{b_2}, \bar{\beta}_{b_2}; -k + Q_{b_1}, \beta_{b_2}) \\ &\quad \cdot f_{\Delta}(k - Q_{b_1} + Q_{b_2}, \gamma_{b_3}; -k + Q_{b_1} - Q_{b_2} + Q_{b_3}, \bar{\gamma}_{b_3}) \cdot f_{\Delta}^*(k, \eta_{b_4}; -k + Q_{b_1} - Q_{b_2} + Q_{b_3}, \eta_{b_4}) \end{aligned} \quad (\text{E21})$$

With the constraint $Q_{b_1} - Q_{b_2} + Q_{b_3} - Q_{b_4} = 0$, we can divide the fourth-order term into several parts. When $b_1 = b_2 = b_3 = b_4 = b$:

$$\begin{aligned} &-\frac{1}{2} \sum_b |\psi_b|^4 \sum_{\alpha_b, \beta_b, \gamma_b, \eta_b} \sum_k G_{0,k}^{\bar{\eta}_b, \alpha_b} G_{0,-k+Q_b}^{\beta_b, \bar{\alpha}_b} G_{0,k}^{\bar{\beta}_b, \gamma_b} G_{0,-k+Q_b}^{\eta_b, \bar{\gamma}_b} \\ &\quad \cdot f_{\Delta}(k, \alpha_b; -k + Q_b, \bar{\alpha}_b) \cdot f_{\Delta}^*(k, \bar{\beta}_b; -k + Q_b, \beta_b) \cdot f_{\Delta}(k, \gamma_b; -k + Q_b, \bar{\gamma}_b) \cdot f_{\Delta}^*(k, \eta_b; -k + Q_b, \eta_b) \end{aligned} \quad (\text{E22})$$

When $b_1 = b_2; b_3 = b_4$ and $b_1 \neq b_3$:

$$-\frac{1}{2} \sum_{b_1 \neq b_3} |\psi_{b_1}|^2 |\psi_{b_3}|^2 \sum_{\alpha_{b_1}, \beta_{b_1}, \gamma_{b_3}, \eta_{b_3}} \sum_k G_{0,k}^{\overline{\eta_{b_3}}, \alpha_{b_1}} G_{0,-k+Q_{b_1}}^{\beta_{b_1}, \overline{\alpha_{b_1}}} G_{0,k}^{\overline{\beta_{b_1}}, \gamma_{b_3}} G_{0,-k+Q_{b_3}}^{\eta_{b_3}, \overline{\gamma_{b_3}}} \cdot f_{\Delta}(k, \alpha_{b_1}; -k + Q_{b_1}, \overline{\alpha_{b_1}}) \cdot f_{\Delta}^*(k, \overline{\beta_{b_1}}; -k + Q_{b_1}, \beta_{b_1}) \cdot f_{\Delta}(k, \gamma_{b_3}; -k + Q_{b_3}, \overline{\gamma_{b_3}}) \cdot f_{\Delta}^*(k, \overline{\eta_{b_3}}; -k + Q_{b_3}, \eta_{b_3}) \quad (\text{E23})$$

When $b_1 = b_4; b_3 = b_2$ and $b_1 \neq b_3$:

$$-\frac{1}{2} \sum_{b_1 \neq b_3} |\psi_{b_1}|^2 |\psi_{b_3}|^2 \sum_{\alpha_{b_1}, \beta_{b_3}, \gamma_{b_3}, \eta_{b_1}} \sum_k G_{0,k}^{\overline{\eta_{b_1}}, \alpha_{b_1}} G_{0,-k+Q_{b_1}}^{\beta_{b_3}, \overline{\alpha_{b_1}}} G_{0,k-Q_{b_1}+Q_{b_3}}^{\overline{\beta_{b_3}}, \gamma_{b_3}} G_{0,-k+Q_{b_1}}^{\eta_{b_1}, \overline{\gamma_{b_3}}} \cdot f_{\Delta}(k, \alpha_{b_1}; -k + Q_{b_1}, \overline{\alpha_{b_1}}) \cdot f_{\Delta}^*(k - Q_{b_1} + Q_{b_3}, \overline{\beta_{b_3}}; -k + Q_{b_1}, \beta_{b_3}) \cdot f_{\Delta}(k - Q_{b_1} + Q_{b_3}, \gamma_{b_3}; -k + Q_{b_1}, \overline{\gamma_{b_3}}) \cdot f_{\Delta}^*(k, \overline{\eta_{b_1}}; -k + Q_{b_1}, \eta_{b_1}) \quad (\text{E24})$$

It is easy to prove that Eq. E23 and Eq. E24 are the same, and they can be combined as follows:

$$-\sum_{b \neq b'} |\psi_b|^2 |\psi_{b'}|^2 \sum_{\alpha_b, \beta_b, \gamma_{b'}, \eta_{b'}} \sum_k G_{0,k}^{\overline{\eta_{b'}}, \alpha_b} G_{0,-k+Q_b}^{\beta_b, \overline{\alpha_b}} G_{0,k}^{\overline{\beta_b}, \gamma_{b'}} G_{0,-k+Q_{b'}}^{\eta_{b'}, \overline{\gamma_{b'}}} \cdot f_{\Delta}(k, \alpha_b; -k + Q_b, \overline{\alpha_b}) \cdot f_{\Delta}^*(k, \overline{\beta_b}; -k + Q_b, \beta_b) \cdot f_{\Delta}(k, \gamma_{b'}; -k + Q_{b'}, \overline{\gamma_{b'}}) \cdot f_{\Delta}^*(k, \overline{\eta_{b'}}; -k + Q_{b'}, \eta_{b'}) \quad (\text{E25})$$

When $b_1 = b_3 = b; b_4 = b_2 = b'$ and $b \neq b'$:

$$-\frac{1}{2} \sum_{b \neq b'} \psi_b^2 \psi_{b'}^{*2} \sum_{\alpha_b, \beta_{b'}, \gamma_b, \eta_{b'}} \sum_k G_{0,k}^{\overline{\eta_{b'}}, \alpha_b} G_{0,-k+Q_b}^{\beta_{b'}, \overline{\alpha_b}} G_{0,k-Q_b+Q_{b'}}^{\overline{\beta_{b'}}, \gamma_b} G_{0,-k+Q_{b'}}^{\eta_{b'}, \overline{\gamma_b}} \cdot f_{\Delta}(k, \alpha_b; -k + Q_b, \overline{\alpha_b}) \cdot f_{\Delta}^*(k - Q_b + Q_{b'}, \overline{\beta_{b'}}; -k + Q_b, \beta_{b'}) \cdot f_{\Delta}(k - Q_b + Q_{b'}, \gamma_b; -k + Q_{b'}, \overline{\gamma_b}) \cdot f_{\Delta}^*(k, \overline{\eta_{b'}}; -k + Q_{b'}, \eta_{b'}) \quad (\text{E26})$$

The fourth-order terms given in Eq. E22, Eq. E25, and Eq. E26, correspond to the Feynman diagrams shown in Fig. 18(b),(c) and (d), respectively.

Next, let us add CDW, for which we define the auxiliary fields ϕ_b along the specific bond directions \mathbf{a}_b with $b = 1, 2, 3$. That is $\phi_1^{\text{AB}} = [\phi_1^{\text{BA}}]^* \equiv \phi_1$, $\phi_2^{\text{CB}} = [\phi_2^{\text{BC}}]^* \equiv \phi_2$, $\phi_3^{\text{AC}} = [\phi_3^{\text{CA}}]^* \equiv \phi_3$. In Nambu spinor representation, the CDW matrix χ satisfies the following relations:

$$\chi_{k\uparrow, k \pm Q_b \uparrow}^{\alpha_b, \overline{\alpha_b}} = \phi_b^{\alpha_b \overline{\alpha_b}} \cdot f_{\chi}(k, \alpha_b; k \pm Q_b, \overline{\alpha_b}) \quad (\text{E27})$$

$$\chi_{k\downarrow, k \pm Q_b \downarrow}^{\alpha_b, \overline{\alpha_b}} = [\phi_b^*]^{\alpha_b \overline{\alpha_b}} \cdot [-f_{\chi}^*(k, \alpha_b; k \pm Q_b, \overline{\alpha_b})] \quad (\text{E28})$$

$$f_{\chi}(k \pm Q_b, \overline{\alpha_b}; k, \alpha_b) = f_{\chi}^*(k, \alpha_b; k \pm Q_b, \overline{\alpha_b}) \quad (\text{E29})$$

$$f_{\chi}(k, \alpha_b; k + Q_b, \overline{\alpha_b}) = f_{\chi}(k, \alpha_b; k - Q_b, \overline{\alpha_b}) \quad (\text{E30})$$

Here, for simplicity, we neglect the CDW order on the next-nearest-neighbor bond, and the factor $f_{\chi}(k\alpha_b, k'\overline{\alpha_b})$ can be determined through the specific internal structure of the CDW order under Q_b .

Following the above procedure, we get the GL free energy

$$F = -\frac{T \ln Z}{N} = \frac{4}{V} \sum_b |\phi_b|^2 + \frac{2}{J} \sum_b |\psi_b|^2 - \frac{T}{N} \text{Trln}(\mathcal{G}_0^{-1} + \chi + \Delta) \quad (\text{E31})$$

The last term $\text{Trln}(\mathcal{G}_0^{-1} + \chi + \Delta)$ can be expanded as

$$\begin{aligned} \text{Trln}(\mathcal{G}_0^{-1} + \chi + \Delta) &= \text{Trln}(\mathcal{G}_0^{-1} [1 + \mathcal{G}_0(\chi + \Delta)]) \\ &= \text{Trln}(\mathcal{G}_0^{-1}) + \text{Trln}(1 + \mathcal{G}_0(\chi + \Delta)) \\ &= \text{const.} + \sum_{n=1}^{\infty} \frac{(-1)^{n+1}}{n} \text{Tr}(\mathcal{G}_0 \chi + \mathcal{G}_0 \Delta)^n \end{aligned} \quad (\text{E32})$$

Again, only even orders of Δ are allowed to be nonzero since only Δ is off-diagonal in Nambu space. Therefore, the

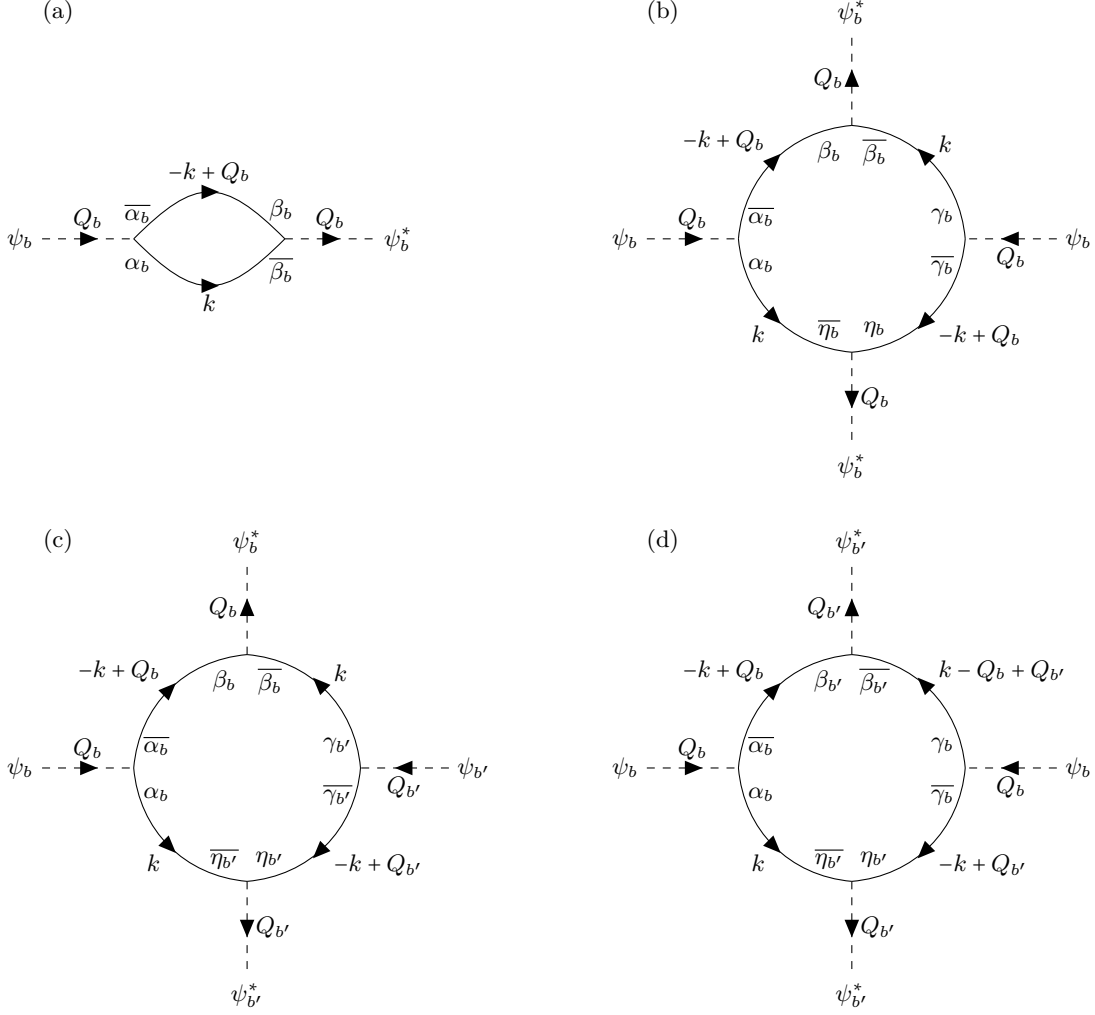


FIG. 18. The Feynman diagrams corresponding to the second-order (a) and fourth-order (b-d) terms in the GL theory, associated with Eq. (2) of the main text, consider only the PDW order. In the diagrams, the dashed lines represent bosonic fields, with their direction indicating either ψ_b^* or ψ_b , and their contribution is given by $f_\Delta^*(k, \alpha_b; k', \bar{\alpha}_b)$ or $f_\Delta(k, \alpha_b; k', \bar{\alpha}_b)$. The solid lines represent the fermionic Green's function $G_0^{\beta\alpha}(k)$, where the sublattice indices of the Green's function are indicated at the endpoints of the lines. The sign of each diagram is determined by $(-1)^{m/2+1}$, where m is the total number of PDW bosonic fields. The coefficient for each diagram corresponds $\frac{c}{m}$, where c is the number of distinct diagrams that can be obtained by performing an overall exchange based on the rotational relation and an overall direction reversal of the bosonic lines labeled b . Diagrams in which b and b' are exchanged are considered equivalent.

lowest-order coupling between PDW and CDW is the third-order,

$$\begin{aligned}
& \frac{1}{3} \cdot 3 \cdot 2 \text{Tr}[\mathcal{G}_{0,\uparrow\uparrow}] \Delta_{\uparrow\downarrow} [\mathcal{G}_{0,\downarrow\downarrow}] \chi_{\downarrow\downarrow} [\mathcal{G}_{0,\downarrow\downarrow}] \Delta_{\downarrow\uparrow} \\
&= 2 \sum_{b1 \neq b2 \neq b3} \sum_{\alpha_{b1}, \beta_{b2}, \gamma_{b3}} \sum_k [\mathcal{G}_{0,\uparrow\uparrow}]_k^{\bar{\gamma}_{b3}, \alpha_{b1}} \Delta_{k\uparrow, -k+Q_{b1}\downarrow}^{\alpha_{b1}, \bar{\alpha}_{b1}} [\mathcal{G}_{0,\downarrow\downarrow}]_{-k+Q_{b1}}^{\bar{\alpha}_{b1}, \beta_{b2}} \chi_{-k+Q_{b1}\downarrow, -k+Q_{b1}-Q_{b2}\downarrow}^{\beta_{b2}, \bar{\beta}_{b2}} [\mathcal{G}_{0,\downarrow\downarrow}]_{-k+Q_{b1}-Q_{b2}}^{\bar{\beta}_{b2}, \gamma_{b3}} \Delta_{-k+Q_{b1}-Q_{b2}\downarrow, k\uparrow}^{\gamma_{b3}, \bar{\gamma}_{b3}} \\
&= -2 \sum_{b \neq b' \neq b''} \sum_{\alpha_b, \beta_{b'}, \gamma_{b''}} \psi_b \psi_{b''}^* [\phi_{b'}^*]^{\beta_{b'}, \bar{\beta}_{b'}} \sum_k G_{0,k}^{\bar{\gamma}_{b'}, \alpha_b} G_{0,-k+Q_b}^{\beta_{b'}, \bar{\alpha}_b} G_{0,-k+Q_b-Q_{b'}}^{\gamma_{b''}, \bar{\beta}_{b''}} \\
&\quad \cdot f_\Delta(k, \alpha_b; -k+Q_b, \bar{\alpha}_b) \cdot f_\chi(-k+Q_b-Q_{b'}, \bar{\beta}_{b''}; -k+Q_b, \beta_{b'}) \cdot f_\Delta^*(k, \bar{\gamma}_{b''}; -k+Q_b-Q_{b'}, \gamma_{b''})
\end{aligned} \tag{E33}$$

$$\tag{E34}$$

The corresponding Feynman diagram is shown in Fig. 19(a). The third-order terms of ϕ contribute to the GL free energy for pure CDW, which have been studied before so we will not discuss them any more.

The fourth-order term is

$$\begin{aligned}
& -\frac{1}{4} [2 \cdot 2 \cdot \text{Tr}[\mathcal{G}_{0,\uparrow\uparrow}] \Delta_{\downarrow\downarrow} [\mathcal{G}_{0,\downarrow\downarrow}] \chi_{\downarrow\downarrow} [\mathcal{G}_{0,\downarrow\downarrow}] \Delta_{\uparrow\uparrow} [\mathcal{G}_{0,\uparrow\uparrow}] \chi_{\uparrow\uparrow} + 4 \cdot 2 \text{Tr}[\mathcal{G}_{0,\uparrow\uparrow}] \Delta_{\downarrow\downarrow} [\mathcal{G}_{0,\downarrow\downarrow}] \Delta_{\uparrow\uparrow} [\mathcal{G}_{0,\uparrow\uparrow}] \chi_{\uparrow\uparrow} [\mathcal{G}_{0,\uparrow\uparrow}] \chi_{\uparrow\uparrow}] \quad (\text{E35}) \\
& = - \sum_{b_1, b_2, b_3, b_4} \sum_{\alpha_{b_1} \beta_{b_2}, \gamma_{b_3}, \eta_{b_4}} \sum_k [\mathcal{G}_{0,\uparrow\uparrow}]_k^{\overline{\eta_{b_4}, \alpha_{b_1}}} \Delta_{k\uparrow, -k+Q_{b_1}\downarrow}^{\alpha_{b_1}, \overline{\alpha_{b_1}}} [\mathcal{G}_{0,\downarrow\downarrow}]_{-k+Q_{b_1}}^{\overline{\alpha_{b_1}, \beta_{b_2}}} \chi_{-k+Q_{b_1}\downarrow, -k+Q_{b_1}-Q_{b_2}\downarrow}^{\beta_{b_2}, \overline{\beta_{b_2}}} \\
& \quad \cdot [\mathcal{G}_{0,\downarrow\downarrow}]_{-k+Q_{b_1}-Q_{b_2}}^{\overline{\beta_{b_2}, \gamma_{b_3}}} \Delta_{-k+Q_{b_1}-Q_{b_2}\downarrow, k-Q_{b_1}+Q_{b_2}+Q_{b_3}\uparrow}^{\gamma_{b_3}, \overline{\gamma_{b_3}}} [\mathcal{G}_{0,\uparrow\uparrow}]_{k-Q_{b_1}+Q_{b_2}+Q_{b_3}}^{\overline{\gamma_{b_3}, \eta_{b_4}}} \chi_{k-Q_{b_1}+Q_{b_2}+Q_{b_3}\uparrow, k\uparrow}^{\eta_{b_4}, \overline{\eta_{b_4}}} \\
& - 2 \sum_{b_1, b_2, b_3, b_4} \sum_{\alpha_{b_1} \beta_{b_2}, \gamma_{b_3}, \eta_{b_4}} \sum_k [\mathcal{G}_{0,\uparrow\uparrow}]_k^{\overline{\eta_{b_4}, \alpha_{b_1}}} \Delta_{k\uparrow, -k+Q_{b_1}\downarrow}^{\alpha_{b_1}, \overline{\alpha_{b_1}}} [\mathcal{G}_{0,\downarrow\downarrow}]_{-k+Q_{b_1}}^{\overline{\alpha_{b_1}, \beta_{b_2}}} \Delta_{-k+Q_{b_1}\downarrow, k-Q_{b_1}+Q_{b_2}\uparrow}^{\beta_{b_2}, \overline{\beta_{b_2}}} \\
& \quad \cdot [\mathcal{G}_{0,\uparrow\uparrow}]_{k-Q_{b_1}+Q_{b_2}}^{\overline{\beta_{b_2}, \gamma_{b_3}}} \chi_{k-Q_{b_1}+Q_{b_2}\uparrow, k-Q_{b_1}+Q_{b_2}-Q_{b_3}\uparrow}^{\gamma_{b_3}, \overline{\gamma_{b_3}}} [\mathcal{G}_{0,\uparrow\uparrow}]_{k-Q_{b_1}+Q_{b_2}-Q_{b_3}}^{\overline{\gamma_{b_3}, \eta_{b_4}}} \chi_{k-Q_{b_1}+Q_{b_2}-Q_{b_3}\uparrow, k\uparrow}^{\eta_{b_4}, \overline{\eta_{b_4}}} \quad (\text{E36})
\end{aligned}$$

In the following, the fourth-order terms in Eq. C1 are given as follows.

When $b_1 = b_2 = b_3 = b_4 = b$, the resulting term of $|\psi_b|^2 |\phi_b|^2$ is given by

$$\begin{aligned}
& \sum_b \sum_{\alpha_b \beta_b, \gamma_b} |\psi_b|^2 |\phi_b|^2 \sum_k G_{0,k}^{\overline{\beta_b, \alpha_b}} G_{0, -k+Q_b}^{\beta_b, \overline{\alpha_b}} G_{0, -k}^{\gamma_b, \overline{\beta_b}} G_{0, k+Q_b}^{\overline{\gamma_b}, \beta_b} \\
& \quad \cdot f_{\Delta}(k, \alpha_b; -k+Q_b, \overline{\alpha_b}) f_{\chi}(-k, \overline{\beta_b}; -k+Q_b, \beta_b) f_{\Delta}^*(k+Q_b, \overline{\gamma_b}; -k, \gamma_b) f_{\chi}(k+Q_b, \beta_b; k, \overline{\beta_b}) \quad (\text{E37})
\end{aligned}$$

$$\begin{aligned}
& + 2 \sum_b \sum_{\alpha_b \beta_b, \gamma_b} |\psi_b|^2 |\phi_b|^2 \sum_k G_k^{\gamma_b, \alpha_b} G_{0, -k+Q_b}^{\beta_b, \overline{\alpha_b}} G_{0, k}^{\overline{\beta_b}, \gamma_b} G_{0, k-Q_b}^{\overline{\gamma_b}, \beta_b} \\
& \quad \cdot f_{\Delta}(k, \alpha_b; -k+Q_b, \overline{\alpha_b}) f_{\Delta}^*(k, \overline{\beta_b}; -k+Q_b, \beta_b) f_{\chi}(k, \gamma_b, k-Q_b, \overline{\gamma_b}) f_{\chi}(k-Q_b, \overline{\beta_b}; k, \gamma_b) \quad (\text{E38})
\end{aligned}$$

For the term of $|\psi_b|^2 |\phi_{b'}|^2$ with $b \neq b'$, the results are

$$\begin{aligned}
& \sum_{b \neq b'} \sum_{\alpha_b \beta_{b'}, \gamma_b} |\psi_b|^2 |\phi_{b'}|^2 \sum_k G_{0,k}^{\overline{\beta_{b'}, \alpha_b}} G_{0, -k+Q_b}^{\beta_{b'}, \overline{\alpha_b}} G_{0, -k+Q_b-Q_{b'}}^{\gamma_b, \overline{\beta_{b'}}} G_{0, k+Q_{b'}}^{\overline{\gamma_b}, \beta_{b'}} \\
& \quad \cdot f_{\Delta}(k, \alpha_b; -k+Q_b, \overline{\alpha_b}) f_{\chi}(-k+Q_b-Q_{b'}, \overline{\beta_{b'}}; -k+Q_b, \beta_{b'}) f_{\Delta}^*(k+Q_{b'}, \overline{\gamma_b}; -k+Q_b-Q_{b'}, \gamma_b) f_{\chi}(k+Q_{b'}, \beta_{b'}; k, \overline{\beta_{b'}}) \quad (\text{E39})
\end{aligned}$$

$$\begin{aligned}
& + 2 \sum_{b \neq b'} \sum_{\alpha_b \beta_b, \gamma_{b'}} |\psi_b|^2 |\phi_{b'}|^2 \sum_k G_{0,k}^{\gamma_{b'}, \alpha_b} G_{0, -k+Q_b}^{\beta_b, \overline{\alpha_b}} G_{0, k}^{\overline{\beta_b}, \gamma_{b'}} G_{0, k-Q_{b'}}^{\overline{\gamma_{b'}}, \beta_{b'}} \\
& \quad \cdot f_{\Delta}(k, \alpha_b; -k+Q_b, \overline{\alpha_b}) f_{\Delta}^*(k, \overline{\beta_b}; -k+Q_b, \beta_b) f_{\chi}(k, \gamma_{b'}, k-Q_{b'}, \overline{\gamma_{b'}}) f_{\chi}(k-Q_{b'}, \overline{\beta_{b'}}; k, \gamma_{b'}) \quad (\text{E40})
\end{aligned}$$

The Eq. E37, E38, E39 and E40 corresponding to the Feynman diagrams shown in Fig. 19(b), (c), (d) and (e) respectively. In addition, there are also other terms like $\psi_1^* \psi_2 \phi_1 \phi_2$, but this effect on PDW has been captured by the third-order coupling term, so we neglect them for simplicity.

-
- | | |
|--|---|
| <p>[1] P. Fulde and R. A. Ferrell, Superconductivity in a strong spin-exchange field, <i>Phys. Rev.</i> 135, A550 (1964).</p> <p>[2] A. I. Larkin and Y. N. Ovchinnikov, Nonuniform state of superconductors, <i>Zh. Eksp. Teor. Fiz.</i> 47, 1136 (1964).</p> <p>[3] M. W. Zwierlein, A. Schirotzek, C. H. Schunck, and W. Ketterle, Fermionic superfluidity with imbalanced spin populations, <i>Science</i> 311, 492 (2006).</p> <p>[4] G. B. Partridge, W. Li, R. I. Kamar, Y. an Liao, and R. G. Hulet, Pairing and phase separation in a polarized fermi gas, <i>Science</i> 311, 503 (2006).</p> <p>[5] L. Radzihovsky and D. E. Sheehy, Imbalanced feshbach-resonant fermi gases, <i>Rep. Prog. Phys.</i> 73, 076501 (2010).</p> <p>[6] P. A. Lee, Amperian pairing and the pseudogap phase</p> | <p>of cuprate superconductors, <i>Phys. Rev. X</i> 4, 031017 (2014).</p> <p>[7] E. Fradkin, S. A. Kivelson, and J. M. Tranquada, Colloquium: Theory of intertwined orders in high temperature superconductors, <i>Rev. Mod. Phys.</i> 87, 457 (2015).</p> <p>[8] D. F. Agterberg, J. S. Davis, S. D. Edkins, E. Fradkin, D. J. Van Harlingen, S. A. Kivelson, P. A. Lee, L. Radzihovsky, J. M. Tranquada, and Y. Wang, The physics of pair-density waves: Cuprate superconductors and beyond, <i>Annu. Rev. Condens. Matter Phys.</i> 11, 231 (2020).</p> <p>[9] Q. Li, M. Hücker, G. D. Gu, A. M. Tsvelik, and J. M. Tranquada, Two-dimensional superconducting fluctuations in stripe-ordered $\text{La}_{1.875}\text{Ba}_{0.125}\text{CuO}_4$, <i>Phys. Rev.</i></p> |
|--|---|

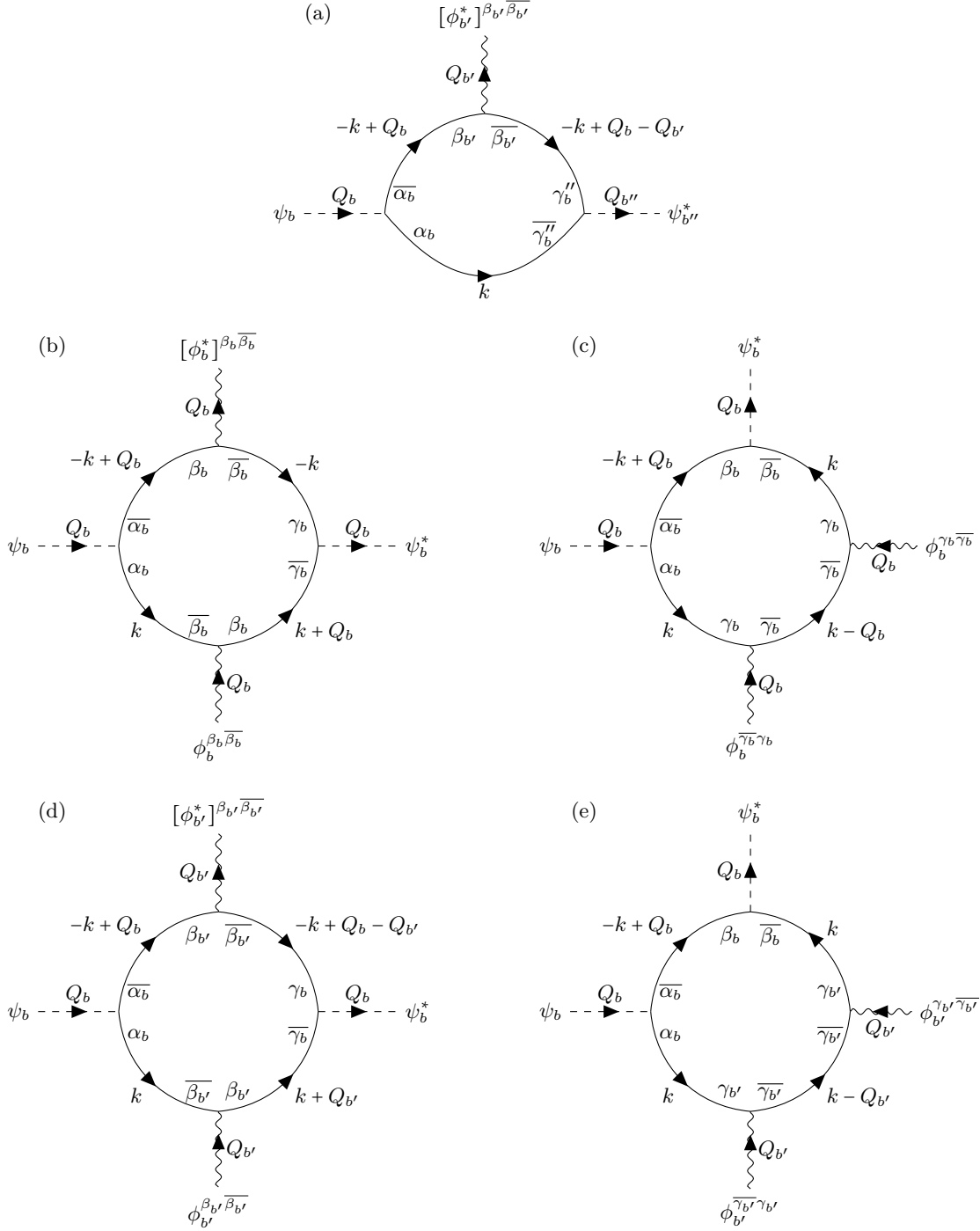


FIG. 19. The Feynman diagrams corresponding to the third-order (a) and fourth-order (b-e) terms in the GL theory, associated with Eq. C1, consider both CDW and PDW orders. In the diagrams, the solid lines represent the fermionic Green's function $G_0^{\beta\alpha}(k)$, where the sublattice indices of the Green's function are indicated at the endpoints of the lines. The dashed lines represent PDW bosonic fields, with their direction indicating either ψ_b^* or ψ_b , contributing $f_\Delta(k, \alpha_b; k', \bar{\alpha}_b)$ or $f_\Delta(k, \alpha_b; k', \bar{\alpha}_b)$. The wavy lines represent CDW bosonic fields, with their direction indicating either ϕ_b^* or ϕ_b , contributing $f_\chi(k, \alpha_b; k', \bar{\alpha}_b)$, where k denotes the outgoing momentum. The sign of each diagram is determined by $(-1)^{m/2+n+1}$, where m is the total number of PDW bosonic fields and n is the total number of PDW and CDW bosonic fields. The coefficient for each diagram corresponds to $\frac{c}{n}$, where c is the number of distinct diagrams that can be obtained by performing an overall exchange based on the rotational relation and an overall direction reversal of the PDW and CDW bosonic lines labeled b . Diagrams in which b and b' are exchanged are considered equivalent.

- Lett.* **99**, 067001 (2007).
- [10] E. Berg, E. Fradkin, E.-A. Kim, S. A. Kivelson, V. Oganesyan, J. M. Tranquada, and S. C. Zhang, Dynamical layer decoupling in a stripe-ordered high- T_c superconductor, *Phys. Rev. Lett.* **99**, 127003 (2007).
- [11] D. F. Agterberg and H. Tsunetsugu, Dislocations and vortices in pair-density-wave superconductors, *Nat. Phys.* **4**, 639 (2008).
- [12] E. Berg, E. Fradkin, and S. A. Kivelson, Charge-4e superconductivity from pair-density-wave order in certain high-temperature superconductors, *Nat. Phys.* **5**, 830 (2009).
- [13] M. H. Hamidian, S. D. Edkins, S. H. Joo, A. Kostin, H. Eisaki, S. Uchida, M. J. Lawler, E.-A. Kim, A. P. Mackenzie, K. Fujita, J. Lee, and J. C. S. Davis, Detection of a Cooper-pair density wave in $\text{Bi}_2\text{Sr}_2\text{CaCu}_2\text{O}_{8+x}$, *Nature* **532**, 343 (2016).
- [14] W. Ruan, X. Li, C. Hu, Z. Hao, H. Li, P. Cai, X. Zhou, D.-H. Lee, and Y. Wang, Visualization of the periodic modulation of Cooper pairing in a cuprate superconductor, *Nat. Phys.* **14**, 1178 (2018).
- [15] S. D. Edkins, A. Kostin, K. Fujita, A. P. Mackenzie, H. Eisaki, S. Uchida, S. Sachdev, M. J. Lawler, E.-A. Kim, J. C. S. Davis, and M. H. Hamidian, Magnetic field-induced pair density wave state in the cuprate vortex halo, *Science* **364**, 976 (2019).
- [16] Z. Shi, P. G. Baity, J. Terzic, T. Sasagawa, and D. Popović, Pair density wave at high magnetic fields in cuprates with charge and spin orders, *Nat. Commun.* **11**, 3323 (2020).
- [17] Z. Du, H. Li, S. H. Joo, E. P. Donoway, J. Lee, J. C. S. Davis, G. Gu, P. D. Johnson, and K. Fujita, Imaging the energy gap modulations of the cuprate pair-density-wave state, *Nature* **580**, 65 (2020).
- [18] X. Li, C. Zou, Y. Ding, H. Yan, S. Ye, H. Li, Z. Hao, L. Zhao, X. Zhou, and Y. Wang, Evolution of charge and pair density modulations in overdoped $\text{Bi}_2\text{Sr}_2\text{CuO}_{6+\delta}$, *Phys. Rev. X* **11**, 011007 (2021).
- [19] S. Wang, P. Choubey, Y. X. Chong, W. Chen, W. Ren, H. Eisaki, S. Uchida, P. J. Hirschfeld, and J. C. S. Davis, Scattering interference signature of a pair density wave state in the cuprate pseudogap phase, *Nat. Commun.* **12**, 6087 (2021).
- [20] C.-W. Cho, J. H. Yang, N. F. Q. Yuan, J. Shen, T. Wolf, and R. Lortz, Thermodynamic evidence for the fulde-ferrell-larkin-ovchinnikov state in the KFe_2As_2 superconductor, *Phys. Rev. Lett.* **119**, 217002 (2017).
- [21] Y. Liu, T. Wei, G. He, Y. Zhang, Z. Wang, and J. Wang, Pair density wave state in a monolayer high- T_c iron-based superconductor, *Nature* **618**, 934 (2023).
- [22] H. Zhao, R. Blackwell, M. Thinel, T. Handa, S. Ishida, X. Zhu, A. Iyo, H. Eisaki, A. N. Pasupathy, and K. Fujita, Smectic pair-density-wave order in $\text{EuRbFe}_4\text{As}_4$, *Nature* **618**, 940 (2023).
- [23] Q. Gu, J. P. Carroll, S. Wang, S. Ran, C. Broyles, H. Siddiquee, N. P. Butch, S. R. Saha, J. Paglione, J. C. S. Davis, and X. Liu, Detection of a pair density wave state in UTe_2 , *Nature* **618**, 921 (2023).
- [24] A. Aishwarya, J. May-Mann, A. Raghavan, L. Nie, M. Romanelli, S. Ran, S. R. Saha, J. Paglione, N. P. Butch, E. Fradkin, and V. Madhavan, Magnetic-field-sensitive charge density waves in the superconductor UTe_2 , *Nature* **618**, 928 (2023).
- [25] H. Chen, H. Yang, B. Hu, Z. Zhao, J. Yuan, Y. Xing, G. Qian, Z. Huang, G. Li, Y. Ye, S. Ma, S. Ni, H. Zhang, Q. Yin, C. Gong, Z. Tu, H. Lei, H. Tan, S. Zhou, C. Shen, X. Dong, B. Yan, Z. Wang, and H.-J. Gao, Roton pair density wave in a strong-coupling kagome superconductor, *Nature* **599**, 222 (2021).
- [26] C. C. Agosta, Inhomogeneous superconductivity in organic and related superconductors, *Crystals* **8**, 285 (2018).
- [27] X. Liu, Y. X. Chong, R. Sharma, and J. C. S. Davis, Discovery of a cooper-pair density wave state in a transition-metal dichalcogenide, *Science* **372**, 1447 (2021).
- [28] E. Berg, E. Fradkin, E.-A. Kim, S. A. Kivelson, V. Oganesyan, J. M. Tranquada, and S. C. Zhang, Dynamical Layer Decoupling in a Stripe-Ordered High- T_c Superconductor, *Phys. Rev. Lett.* **99**, 127003 (2007).
- [29] E. Berg, E. Fradkin, S. A. Kivelson, and J. M. Tranquada, Striped superconductors: how spin, charge and superconducting orders intertwine in the cuprates, *New J. Phys.* **11**, 115004 (2009).
- [30] P. A. Lee, Amperean Pairing and the Pseudogap Phase of Cuprate Superconductors, *Phys. Rev. X* **4**, 031017 (2014).
- [31] G. Y. Cho, R. Soto-Garrido, and E. Fradkin, Topological pair-density-wave superconducting states, *Phys. Rev. Lett.* **113**, 256405 (2014).
- [32] Y. Wang, D. F. Agterberg, and A. Chubukov, Coexistence of charge-density-wave and pair-density-wave orders in underdoped cuprates, *Phys. Rev. Lett.* **114**, 197001 (2015).
- [33] Y. Wang, S. D. Edkins, M. H. Hamidian, J. C. S. Davis, E. Fradkin, and S. A. Kivelson, Pair density waves in superconducting vortex halos, *Phys. Rev. B* **97**, 174510 (2018).
- [34] J.-T. Jin, K. Jiang, H. Yao, and Y. Zhou, Interplay between pair density wave and a nested fermi surface, *Phys. Rev. Lett.* **129**, 167001 (2022).
- [35] S. Zhou and Z. Wang, Chern fermi pocket, topological pair density wave, and charge-4e and charge-6e superconductivity in kagomé superconductors, *Nat. Commun.* **13**, 7288 (2022).
- [36] S.-C. Zhang, Recent developments in the $\text{SO}(5)$ theory of high T_c superconductivity, *J. Phys. Chem. Solids* **59**, 1774 (1998).
- [37] A. Himeda, T. Kato, and M. Ogata, Stripe States with Spatially Oscillating d -Wave Superconductivity in the Two-Dimensional $t-t'-J$ Model, *Phys. Rev. Lett.* **88**, 117001 (2002).
- [38] M. Raczkowski, M. Capello, D. Poilblanc, R. Frésard, and A. M. Oleś, Unidirectional d -wave superconducting domains in the two-dimensional $t-J$ model, *Phys. Rev. B* **76**, 140505 (2007).
- [39] M. Capello, M. Raczkowski, and D. Poilblanc, Stability of rvb hole stripes in high-temperature superconductors, *Phys. Rev. B* **77**, 224502 (2008).
- [40] K.-Y. Yang, W. Q. Chen, T. M. Rice, M. Sigrist, and F.-C. Zhang, Nature of stripes in the generalized $t-J$ model applied to the cuprate superconductors, *New J. Phys.* **11**, 055053 (2009).
- [41] F. Loder, A. P. Kampf, and T. Kopp, Superconducting state with a finite-momentum pairing mechanism in zero external magnetic field, *Phys. Rev. B* **81**, 020511 (2010).
- [42] E. Berg, E. Fradkin, and S. A. Kivelson, Pair-density-wave correlations in the kondo-heisenberg model, *Phys.*

- Rev. Lett.* **105**, 146403 (2010).
- [43] F. Loder, S. Graser, A. P. Kampf, and T. Kopp, Mean-field pairing theory for the charge-stripe phase of high-temperature cuprate superconductors, *Phys. Rev. Lett.* **107**, 187001 (2011).
- [44] A. Jaefari and E. Fradkin, Pair-density-wave superconducting order in two-leg ladders, *Phys. Rev. B* **85**, 035104 (2012).
- [45] R. Soto-Garrido and E. Fradkin, Pair-density-wave superconducting states and electronic liquid-crystal phases, *Phys. Rev. B* **89**, 165126 (2014).
- [46] R. Soto-Garrido, G. Y. Cho, and E. Fradkin, Quasi-one-dimensional pair density wave superconducting state, *Phys. Rev. B* **91**, 195102 (2015).
- [47] J. Wårdh and M. Granath, Effective model for a supercurrent in a pair-density wave, *Phys. Rev. B* **96**, 224503 (2017).
- [48] J. Wårdh, B. M. Andersen, and M. Granath, Suppression of superfluid stiffness near a lifshitz-point instability to finite-momentum superconductivity, *Phys. Rev. B* **98**, 224501 (2018).
- [49] T. Sarkar, R. L. Greene, and S. Das Sarma, Anomalous normal-state resistivity in superconducting $\text{La}_{2-x}\text{Ce}_x\text{CuO}_4$: Fermi liquid or strange metal?, *Phys. Rev. B* **98**, 224503 (2018).
- [50] X. Y. Xu, K. T. Law, and P. A. Lee, Pair density wave in the doped t - J model with ring exchange on a triangular lattice, *Phys. Rev. Lett.* **122**, 167001 (2019).
- [51] K. S. Huang, Z. Han, S. A. Kivelson, and H. Yao, Pair-density-wave in the strong coupling limit of the Holstein-Hubbard model, *npj Quantum Mater.* **7**, 17 (2022).
- [52] Z. Han and S. A. Kivelson, Pair density wave and reentrant superconducting tendencies originating from valley polarization, *Phys. Rev. B* **105**, L100509 (2022).
- [53] Y.-M. Wu, P. A. Nosov, A. A. Patel, and S. Raghu, Pair density wave order from electron repulsion, *Phys. Rev. Lett.* **130**, 026001 (2023).
- [54] Z. Wu, Y.-M. Wu, and F. Wu, Pair density wave and loop current promoted by van hove singularities in moiré systems, *Phys. Rev. B* **107**, 045122 (2023).
- [55] Y.-M. Wu, Z. Wu, and H. Yao, Pair-density-wave and chiral superconductivity in twisted bilayer transition metal dichalcogenides, *Phys. Rev. Lett.* **130**, 126001 (2023).
- [56] C. Setty, L. Fanfarillo, and P. J. Hirschfeld, Mechanism for fluctuating pair density wave, *Nat. Commun.* **14**, 3181 (2023).
- [57] H.-C. Jiang, Pair density wave in the doped three-band hubbard model on two-leg square cylinders, *Phys. Rev. B* **107**, 214504 (2023).
- [58] D. Shaffer, F. J. Burnell, and R. M. Fernandes, Weak-coupling theory of pair density wave instabilities in transition metal dichalcogenides, *Phys. Rev. B* **107**, 224516 (2023).
- [59] D. Shaffer and L. H. Santos, Triplet pair density wave superconductivity on the π -flux square lattice, *Phys. Rev. B* **108**, 035135 (2023).
- [60] Y.-F. Jiang and H. Yao, Pair-density-wave superconductivity: A microscopic model on the 2d honeycomb lattice, *Phys. Rev. Lett.* **133**, 176501 (2024).
- [61] Y.-M. Wu, R. Thomale, and S. Raghu, Sublattice interference promotes pair density wave order in kagome metals, *Phys. Rev. B* **108**, L081117 (2023).
- [62] H.-K. Zhang, R.-Y. Sun, and Z.-Y. Weng, Pair density wave characterized by a hidden string order parameter, *Phys. Rev. B* **108**, 115136 (2023).
- [63] F. Chen and D. N. Sheng, Singlet, triplet, and pair density wave superconductivity in the doped triangular-lattice moiré system, *Phys. Rev. B* **108**, L201110 (2023).
- [64] C. Setty, J. Zhao, L. Fanfarillo, E. W. Huang, P. J. Hirschfeld, P. W. Phillips, and K. Yang, Exact solution for finite center-of-mass momentum cooper pairing, *Phys. Rev. B* **108**, 174506 (2023).
- [65] H.-C. Jiang and T. P. Devereaux, Pair density wave and superconductivity in a kinetically frustrated doped Emery model on a square lattice, *Front. Electron. Mater.* **3**, 1323404 (2023).
- [66] F. Liu and Z. Han, Pair density wave and $s \pm id$ superconductivity in a strongly coupled lightly doped kondo insulator, *Phys. Rev. B* **109**, L121101 (2024).
- [67] A. Bose, S. Vadnais, and A. Paramakanti, Altermagnetism and superconductivity in a multiorbital $t - J$ model, *Phys. Rev. B* **110**, 205120 (2024).
- [68] J. Wang, W. Sun, H.-X. Wang, Z. Han, S. A. Kivelson, and H. Yao, Pair density waves in the strong-coupling two-dimensional holstein-hubbard model: a variational monte carlo study (2024), [arXiv:2404.11950](https://arxiv.org/abs/2404.11950) [cond-mat.str-el].
- [69] B. R. Ortiz, L. C. Gomes, J. R. Morey, M. Winiarski, M. Bordelon, J. S. Mangum, I. W. H. Oswald, J. A. Rodriguez-Rivera, J. R. Neilson, S. D. Wilson, E. Ertekin, T. M. McQueen, and E. S. Toberer, New kagome prototype materials: discovery of KV_3Sb_5 , RbV_3Sb_5 , and CsV_3Sb_5 , *Phys. Rev. Mater.* **3**, 094407 (2019).
- [70] B. R. Ortiz, S. M. L. Teicher, Y. Hu, J. L. Zuo, P. M. Sarte, E. C. Schueller, A. M. M. Abeykoon, M. J. Krogstad, S. Rosenkranz, R. Osborn, R. Seshadri, L. Balents, J. He, and S. D. Wilson, CsV_3Sb_5 : A \mathbb{Z}_2 Topological Kagome Metal with a Superconducting Ground State, *Phys. Rev. Lett.* **125**, 247002 (2020).
- [71] N. Shumiya, M. S. Hossain, J.-X. Yin, Y.-X. Jiang, B. R. Ortiz, H. Liu, Y. Shi, Q. Yin, H. Lei, S. S. Zhang, G. Chang, Q. Zhang, T. A. Cochran, D. Multer, M. Litskevich, Z.-J. Cheng, X. P. Yang, Z. Guguchia, S. D. Wilson, and M. Z. Hasan, Intrinsic nature of chiral charge order in the kagome superconductor RbV_3Sb_5 , *Phys. Rev. B* **104**, 035131 (2021).
- [72] B. R. Ortiz, P. M. Sarte, E. M. Kenney, M. J. Graf, S. M. L. Teicher, R. Seshadri, and S. D. Wilson, Superconductivity in the \mathbb{Z}_2 kagome metal KV_3Sb_5 , *Phys. Rev. Mater.* **5**, 034801 (2021).
- [73] J.-X. Yin, B. Lian, and M. Z. Hasan, Topological kagome magnets and superconductors, *Nature* **612**, 647 (2022).
- [74] T. Neupert, M. M. Denner, J.-X. Yin, R. Thomale, and M. Z. Hasan, Charge order and superconductivity in kagome materials, *Nat. Phys.* **18**, 137 (2022).
- [75] K. Jiang, T. Wu, J.-X. Yin, Z. Wang, M. Z. Hasan, S. D. Wilson, X. Chen, and J. Hu, Kagome superconductors AV_3Sb_5 ($A = \text{K}, \text{Rb}, \text{Cs}$), *Natl. Sci. Rev.* **10**, nwac199 (2023).
- [76] S. D. Wilson and B. R. Ortiz, AV_3Sb_5 kagome superconductors, *Nat. Rev. Mater.* **9**, 420 (2024).
- [77] S.-L. Yu and J.-X. Li, Chiral superconducting phase and chiral spin-density-wave phase in a hubbard model on the kagome lattice, *Phys. Rev. B* **85**, 144402 (2012).

- [78] M. L. Kiesel and R. Thomale, Sublattice interference in the kagome hubbard model, *Phys. Rev. B* **86**, 121105 (2012).
- [79] W.-S. Wang, Z.-Z. Li, Y.-Y. Xiang, and Q.-H. Wang, Competing electronic orders on kagome lattices at van hove filling, *Phys. Rev. B* **87**, 115135 (2013).
- [80] M. L. Kiesel, C. Platt, and R. Thomale, Unconventional fermi surface instabilities in the kagome hubbard model, *Phys. Rev. Lett.* **110**, 126405 (2013).
- [81] J.-W. Dong, Z. Wang, and S. Zhou, Loop-current charge density wave driven by long-range coulomb repulsion on the kagomé lattice, *Phys. Rev. B* **107**, 045127 (2023).
- [82] Q.-G. Yang, M. Yao, D. Wang, and Q.-H. Wang, Charge bond order and *s*-wave superconductivity in the kagome lattice with electron-phonon coupling and electron-electron interaction, *Phys. Rev. B* **109**, 075130 (2024).
- [83] Y.-Q. Liu, Y.-B. Liu, W.-S. Wang, D. Wang, and Q.-H. Wang, Electronic orders on the kagome lattice at the lower van hove filling, *Phys. Rev. B* **109**, 075127 (2024).
- [84] See Supplemental Material at [URL] for theoretical technique details, further numerical results, and a microscopic derivations of the GL theory. The Supplemental Material also contains Refs. [101–105].
- [85] A. Mine, Y. Zhong, J. Liu, T. Suzuki, S. Najafzadeh, T. Uchiyama, J.-X. Yin, X. Wu, X. Shi, Z. Wang, Y. Yao, and K. Okazaki, Direct observation of anisotropic cooper pairing in kagome superconductor CsV₃Sb₅ (2024), [arXiv:2404.18472](https://arxiv.org/abs/2404.18472) [cond-mat.supr-con].
- [86] U. Sivan and Y. Imry, Multichannel landauer formula for thermoelectric transport with application to thermopower near the mobility edge, *Phys. Rev. B* **33**, 551 (1986).
- [87] X. Feng, K. Jiang, Z. Wang, and J. Hu, Chiral flux phase in the kagome superconductor AV₃Sb₅, *Science Bulletin* **66**, 1384 (2021).
- [88] M. M. Denner, R. Thomale, and T. Neupert, Analysis of charge order in the kagome metal AV₃Sb₅ (*A* = K, Rb, Cs), *Phys. Rev. Lett.* **127**, 217601 (2021).
- [89] Y.-P. Lin and R. M. Nandkishore, Complex charge density waves at Van Hove singularity on hexagonal lattices: Haldane-model phase diagram and potential realization in the kagome metals AV₃Sb₅ (*A*=K, Rb, Cs), *Phys. Rev. B* **104**, 045122 (2021).
- [90] T. Park, M. Ye, and L. Balents, Electronic instabilities of kagome metals: Saddle points and landau theory, *Phys. Rev. B* **104**, 035142 (2021).
- [91] M. H. Christensen, T. Birol, B. M. Andersen, and R. M. Fernandes, Theory of the charge density wave in av₃sb₅ kagome metals, *Phys. Rev. B* **104**, 214513 (2021).
- [92] M. H. Christensen, T. Birol, B. M. Andersen, and R. M. Fernandes, Loop currents in AV₃Sb₅ kagome metals: Multipolar and toroidal magnetic orders, *Phys. Rev. B* **106**, 144504 (2022).
- [93] M. Kang, S. Fang, J.-K. Kim, B. R. Ortiz, S. H. Ryu, J. Kim, J. Yoo, G. Sangiovanni, D. Di Sante, B.-G. Park, C. Jozwiak, A. Bostwick, E. Rotenberg, E. Kaxiras, S. D. Wilson, J.-H. Park, and R. Comin, Twofold van Hove singularity and origin of charge order in topological kagome superconductor CsV₃Sb₅, *Nat. Phys.* **18**, 301 (2022).
- [94] Y. Hu, X. Wu, B. R. Ortiz, S. Ju, X. Han, J. Ma, N. C. Plumb, M. Radovic, R. Thomale, S. D. Wilson, A. P. Schnyder, and M. Shi, Rich nature of Van Hove singularities in Kagome superconductor CsV₃Sb₅, *Nat. Commun.* **13**, 2220 (2022).
- [95] H. Li, D. Oh, M. Kang, H. Zhao, B. R. Ortiz, Y. Oey, S. Fang, Z. Ren, C. Jozwiak, A. Bostwick, E. Rotenberg, J. G. Checkelsky, Z. Wang, S. D. Wilson, R. Comin, and I. Zeljkovic, Small fermi pockets intertwined with charge stripes and pair density wave order in a kagome superconductor, *Phys. Rev. X* **13**, 031030 (2023).
- [96] Y. Hu, X. Wu, A. P. Schnyder, and M. Shi, Electronic landscape of kagome superconductors AV₃Sb₅ (*A* = K, Rb, Cs) from angle-resolved photoemission spectroscopy, *npj Quantum Mater.* **8**, 67 (2023).
- [97] H. Deng, H. Qin, G. Liu, T. Yang, R. Fu, Z. Zhang, X. Wu, Z. Wang, Y. Shi, J. Liu, H. Liu, X.-Y. Yan, W. Song, X. Xu, Y. Zhao, M. Yi, G. Xu, H. Hohmann, S. C. Holbek, M. Dürrnagel, S. Zhou, G. Chang, Y. Yao, Q. Wang, Z. Guguchia, T. Neupert, R. Thomale, M. H. Fischer, and J.-X. Yin, Chiral kagome superconductivity modulations with residual Fermi arcs, *Nature* **632**, 775 (2024).
- [98] M. Sigrist, T. M. Rice, and K. Ueda, Low-field magnetic response of complex superconductors, *Phys. Rev. Lett.* **63**, 1727 (1989).
- [99] E. Babaev, Vortices with Fractional Flux in Two-Gap Superconductors and in Extended Faddeev Model, *Phys. Rev. Lett.* **89**, 067001 (2002).
- [100] J. Ge, P. Wang, Y. Xing, Q. Yin, A. Wang, J. Shen, H. Lei, Z. Wang, and J. Wang, Charge-4*e* and charge-6*e* flux quantization and higher charge superconductivity in kagome superconductor ring devices, *Phys. Rev. X* **14**, 021025 (2024).
- [101] J. Šmakov, I. Martin, and A. V. Balatsky, Josephson scanning tunneling microscopy, *Phys. Rev. B* **64**, 212506 (2001).
- [102] Y.-X. Jiang, J.-X. Yin, M. M. Denner, N. Shumiya, B. R. Ortiz, G. Xu, Z. Guguchia, J. He, M. S. Hossain, X. Liu, *et al.*, Unconventional chiral charge order in kagome superconductor KV₃Sb₅, *Nat. Mater.* **20**, 1353 (2021).
- [103] H.-S. Xu, Y.-J. Yan, R. Yin, W. Xia, S. Fang, Z. Chen, Y. Li, W. Yang, Y. Guo, and D.-L. Feng, Multiband superconductivity with sign-preserving order parameter in kagome superconductor CsV₃Sb₅, *Phys. Rev. Lett.* **127**, 187004 (2021).
- [104] H. Zhao, H. Li, B. R. Ortiz, S. M. Teicher, T. Park, M. Ye, Z. Wang, L. Balents, S. D. Wilson, and I. Zeljkovic, Cascade of correlated electron states in the kagome superconductor CsV₃Sb₅, *Nature* **599**, 216 (2021).
- [105] Y. Luo, Y. Han, J. Liu, H. Chen, Z. Huang, L. Huai, H. Li, B. Wang, J. Shen, S. Ding, Z. Li, S. Peng, Z. Wei, Y. Miao, X. Sun, Z. Ou, Z. Xiang, M. Hashimoto, D. Lu, Y. Yao, H. Yang, X. Chen, H.-J. Gao, Z. Qiao, Z. Wang, and J. He, A unique van Hove singularity in kagome superconductor CsV_{3-x}Ta_xSb₅ with enhanced superconductivity, *Nat. Commun.* **14**, 3819 (2023).